Citation for final published version:

Publishers page: https://doi.org/10.3847/1538-4357/acc85c

CrossMark

BICEP/Keck. XVII. Line-of-sight Distortion Analysis: Estimates of Gravitational Lensing, Anisotropic Cosmic Birefringence, Patchy Reionization, and Systematic Errors

P. A. R. Ade[1], Z. Ahmed[2], M. Amiri[3], D. Barkats[4], R. Basu Thakur[5], C. A. Bischoff[6], D. Beck[2,7], J. J. Bock[5,8], H. Boenish[4],
E. Bullock[9], V. Buza[10], J. R. Cheshire IV[9], J. Connors[4], J. Cornelison[4], M. Crumrine[11], A. Cukierman[2,5,7], E. V. Denison[12],
M. Dierickx[4], L. Duband[13], M. Eiben[4], S. Fatigoni[3], J. P. Filippini[14,15], S. Fliescher[11], C. Giannakopoulos[6],
N. Goeckner-Wald[7], D. C. Goldfinger[4], J. Grayson[7], P. Grimes[4], G. Hall[11], G. Halal[7], M. Halpern[3], E. Hand[6],
S. Harrison[4], S. Henderson[2], S. R. Hildebrandt[5,8], J. Hubmayr[12], H. Hui[5], K. D. Irwin[2,7,12], J. Kang[5,7], K. S. Karkare[4,10],
E. Karpel[7], S. Kefeli[5], S. A. Kernasovskiy[7], J. M. Kovac[4,16], C. L. Kuo[2,7], K. Lau[11], E. M. Leitch[10], A. Lennox[14],
K. G. Megerian[8], L. Minutolo[5], L. Moncelsi[5], Y. Nakato[7], T. Namikawa[17], H. T. Nguyen[8], R. O'Brient[5,8], R. W. Ogburn IV[2,7],
S. Palladino[6], M. Petroff[4], T. Prouve[13], C. Pryke[9,11], B. Racine[4,18], C. D. Reintsema[12], S. Richter[4], A. Schillaci[5],
R. Schwarz[11], B. L. Schmitt[4], C. D. Sheehy[19], B. Singari[9], A. Soliman[5], T. St. Germaine[4,16], B. Steinbach[5], R. V. Sudiwala[1],
G. P. Teply[5], K. L. Thompson[2,7], J. E. Tolan[7], C. Tucker[1], A. D. Turner[8], C. Umiltà[6,14], C. Vergès[4], A. G. Vieregg[10,20],
A. Wandui[5], A. C. Weber[8], D. V. Wiebe[3], J. Willmert[11], C. L. Wong[4,16], W. L. K. Wu[2], H. Yang[7], K. W. Yoon[2,7], E. Young[2,7],
C. Yu[7], L. Zeng[4], C. Zhang[5], and S. Zhang[5]
BICEP/Keck Collaboration
[1] School of Physics and Astronomy, Cardiff University, Cardiff, CF24 3AA, UK
[2] Kavli Institute for Particle Astrophysics and Cosmology, SLAC National Accelerator Laboratory, 2575 Sand Hill Road, Menlo Park, CA 94025, USA
[3] Department of Physics and Astronomy, University of British Columbia, Vancouver, BC, V6T 1Z1, Canada
[4] Center for Astrophysics, Harvard & Smithsonian, Cambridge, MA 02138, USA
[5] Department of Physics, California Institute of Technology, Pasadena, CA 91125, USA
[6] Department of Physics, University of Cincinnati, Cincinnati, OH 45221, USA
[7] Department of Physics, Stanford University, Stanford, CA 94305, USA; iameric@stanford.edu
[8] Jet Propulsion Laboratory, Pasadena, CA 91109, USA
[9] Minnesota Institute for Astrophysics, University of Minnesota, Minneapolis, MN 55455, USA
[10] Kavli Institute for Cosmological Physics, University of Chicago, Chicago, IL 60637, USA
[11] School of Physics and Astronomy, University of Minnesota, Minneapolis, MN 55455, USA
[12] National Institute of Standards and Technology, Boulder, CO 80305, USA
[13] Service des Basses Températures, Commissariat à l'Energie Atomique, F-38054 Grenoble, France
[14] Department of Physics, University of Illinois at Urbana-Champaign, Urbana, IL 61801, USA
[15] Department of Astronomy, University of Illinois at Urbana-Champaign, Urbana, IL 61801, USA
[16] Department of Physics, Harvard University, Cambridge, MA 02138, USA
[17] Kavli Institute for the Physics and Mathematics of the Universe (WPI), UTIAS, The University of Tokyo, Kashiwa, Chiba 277-8583, Japan
[18] Aix-Marseille Université, CNRS/IN2P3, CPPM, F-13288 Marseille, France
[19] Physics Department, Brookhaven National Laboratory, Upton, NY 11973, USA
[20] Department of Physics, Enrico Fermi Institute, University of Chicago, Chicago, IL 60637, USA

Abstract

We present estimates of line-of-sight distortion fields derived from the 95 and 150 GHz data taken by BICEP2, BICEP3, and the Keck Array up to the 2018 observing season, leading to cosmological constraints and a study of instrumental and astrophysical systematics. Cosmological constraints are derived from three of the distortion fields concerning gravitational lensing from large-scale structure, polarization rotation from magnetic fields or an axion-like field, and the screening effect of patchy reionization. We measure an amplitude of the lensing power spectrum $A_L^{\phi\phi} = 0.95 \pm 0.20$. We constrain polarization rotation, expressed as the coupling constant of a Chern–Simons electromagnetic term $g_{a\gamma} \leqslant 2.6 \times 10^{-2}/H_I$, where H_I is the inflationary Hubble parameter, and an amplitude of primordial magnetic fields smoothed over 1 Mpc $B_{1\mathrm{Mpc}} \leqslant 6.6$ nG at 95 GHz. We constrain the rms of optical depth fluctuations in a simple "crinkly surface" model of patchy reionization, finding $A^\tau < 0.19$ (2σ) for the coherence scale of $L_c = 100$. We show that all of the distortion fields of the 95 and 150 GHz polarization maps are consistent with simulations including lensed ΛCDM, dust, and noise, with no evidence for instrumental systematics. In some cases, the *EB* and *TB* quadratic estimators presented here are more sensitive than our previous map-based null tests at identifying and rejecting spurious *B*-modes that might arise from instrumental effects. Finally, we verify that the standard deprojection filtering in the BICEP/Keck data processing is effective at removing temperature to polarization leakage.

1. Introduction

Even with many orders of magnitude of improvement in the precision of the measurements, primordial cosmic microwave background (CMB) fluctuations remain statistically isotropic, such that their statistics are well described by angular power spectra. On the other hand, multiple secondary effects after recombination distort the primary CMB fluctuations, inducing new correlations among observed CMB fluctuations. Examples include gravitational lensing by large-scale structure (Zaldarriaga & Seljak 1998), patchy reionization that modulates the amplitude of the CMB fields (Hu 2000; Dvorkin et al. 2009), and cosmic birefringence that rotates the CMB polarization angle (Yadav et al. 2012; Marsh 2016). There are also various instrumental systematics that can generate spurious B-modes by distorting the incoming T, Q, and U fields, most notably the temperature to polarization (T to P) leakage caused by beam and gain mismatches (BICEP2 Collaboration III 2015; Keck Array & BICEP2 Collaborations XI 2019) and E to B leakage from errors in polarization angle calibration. A comprehensive investigation of the statistical properties of the temperature and polarization maps can be used as a powerful tool to distinguish the sources of the observed B-modes, deciding whether they are cosmological or instrumental.

The secondary and instrumental effects listed above are similar in that they can be described as distortion effects that mix the Stokes T, Q, and U fields along or around each line-of-sight direction $\hat{n}$. Yadav et al. (2010) characterized distortions of the primordial CMB fluctuations by introducing 11 distortion fields that depend on the line-of-sight direction. The B-modes generated by these map distortions would have correlations with E or T that do not exist in the primordial signal in standard ΛCDM cosmology. Thus, EB and TB correlations can be used to reconstruct the distortion fields and study the physical processes and instrumental systematic effects that are associated with specific types of distortions.

In this paper, we reconstruct the 11 distortion fields by applying the minimum variance EB and TB quadratic estimators derived in Hu & Okamoto (2002) and Yadav et al. (2010) to our observed B-mode signal and use their power spectra $\hat{C}_L^{DD}$ to constrain cosmological models and systematics. We will be referencing the previous publications from the BICEP/Keck (BK) experiments: BICEP2 Collaboration I (2014, hereafter BK-I), BICEP2 Collaboration II (2014, hereafter BK-II), BICEP2 Collaboration III (2015, hereafter BK-III), Keck Array & BICEP2 Collaborations VII (2016, hereafter BK-VII), Keck Array & BICEP2 Collaborations VIII (2016, hereafter BK-VIII), Keck Array & BICEP2 Collaborations IX (2017, hereafter BK-IX), Keck Array & BICEP2 Collaborations X (2018, hereafter BK-X), and BICEP/Keck Collaboration XIII (2021, hereafter BK-XIII).

This paper is organized as follows. In Section 2, we give an overview of the different distortion fields and some background on the cosmological effects that correspond to some of the distortions. In Section 3, we describe our data and simulations used for the distortion field analysis. In Section 4, we outline the analysis method, including how to go from Q and U maps to an unbiased distortion field power spectrum and how to combine the distortion power spectra from two data sets. In Section 5, we use the power spectra of three of the reconstructed distortion fields to set constraints on gravitational lensing, patchy reionization, and cosmic birefringence. In Section 6, we discuss the instrumental effects that could produce distortion effects in our data and test for residual systematic effects in the BK data with the distortion field spectra.

2. Introduction to the Distortion Fields

In Hu et al. (2003), systematic effects in CMB polarization maps are described as modifications to the Stokes Q and U maps by distortions along the line-of-sight $\hat{n}$. Following Yadav et al. (2010), we model these distortions with 11 distortion fields as

$$
\begin{aligned}
\delta[Q \pm iU](\hat{n}) = &[\tau \pm i2\alpha](\hat{n})[\tilde{Q} \pm i\tilde{U}](\hat{n}) \\
&+ [f_1 \pm if_2](\hat{n})[\tilde{Q} \mp i\tilde{U}](\hat{n}) \\
&+ [\gamma_1 \pm i\gamma_2](\hat{n})\tilde{T}(\hat{n}) \\
&+ \sigma\boldsymbol{p}(\hat{n}) \cdot \nabla[\tilde{Q} \pm i\tilde{U}](\hat{n}) \\
&+ \sigma[d_1 \pm id_2](\hat{n})[\partial_1 \pm i\partial_2]\tilde{T}(\hat{n}) \\
&+ \sigma^2 q(\hat{n})[\partial_1 \pm i\partial_2]^2\tilde{T}(\hat{n}),
\end{aligned}
\tag{1}
$$

where $\tilde{T}$, $\tilde{Q}$, and $\tilde{U}$ stand for the undistorted primordial CMB intensity and polarization fields. There are 11 terms; $\boldsymbol{p}(\hat{n})$ is a two-dimensional vector. Quantities in the first line correspond to distortions along a unique line of sight, while the second line shows field mixing in the neighborhood of a single line $\hat{n}$. The quantity σ denotes a chosen length scale for these terms and makes the distortion fields unitless. The operators ∂_1 and ∂_2 represent the covariant derivatives along the R.A. and decl. directions, and $\nabla[\tilde{Q} \pm i\tilde{U}]$ is the gradient with components $\partial_i[\tilde{Q} \pm i\tilde{U}]$.

Yadav et al. (2010) further showed that these distortion fields can be estimated directly using quadratic combinations of the data. The filter weights f_{ℓ_1,ℓ_2}^{EB} and f_{ℓ_1,ℓ_2}^{TB} used in the construction of each of the 11 distortions from power spectra are shown in Table 2. Note that this table differs from a similar table in Yadav et al. (2010) in that we use a different notation for pixel- and harmonic-space quantities, denoting the latter with alphabetical instead of numerical subscripts. Also, the weights to construct perturbations to E and B from these distortions have been omitted, since we do not use them. See Appendix A and Section 4 for more details.

Each of the distortion fields can be matched with a specific source, offering a rich phenomenology. The $\tau(\hat{n})$ field describes a modulation of the amplitude of the polarization maps; $\alpha(\hat{n})$ describes the rotation of the polarization angle; $f_1(\hat{n})$ and $f_2(\hat{n})$ describe the coupling between the two polarization field spin states; the components of $\boldsymbol{p}(\hat{n})$, $p_1(\hat{n})$, and $p_2(\hat{n})$ describe the change in photon direction; $\gamma_1(\hat{n})$ and $\gamma_2(\hat{n})$ describe monopole T to P leakage; $d_1(\hat{n})$ and $d_2(\hat{n})$ describe dipole T to P leakage; and $q(\hat{n})$ describes quadrupole T to P leakage. All 11 distortion fields can correspond to specific potential instrumental systematic effects. We will discuss them in depth in that context in Section 6.

Among the distortion fields in Equation (1), there are three that correspond to known or conjectured cosmological signals. These are $\boldsymbol{p}(\hat{n})$, change of direction of the CMB photons; $\tau(\hat{n})$, amplitude modulation; and $\alpha(\hat{n})$, rotation of the plane of linear polarization.

The CMB photons traveling from the last scattering surface are deflected by the intervening matter along the line of sight (Zaldarriaga & Seljak 1998). The change of photon direction, $\boldsymbol{p}(\hat{n})$, is referred to as the weak gravitational lensing of the CMB.

The lensing potential is commonly decomposed into gradient and curl lensing potentials, Φ and Ω (Hirata & Seljak 2003; Cooray et al. 2005; Namikawa et al. 2012), such that the lensed
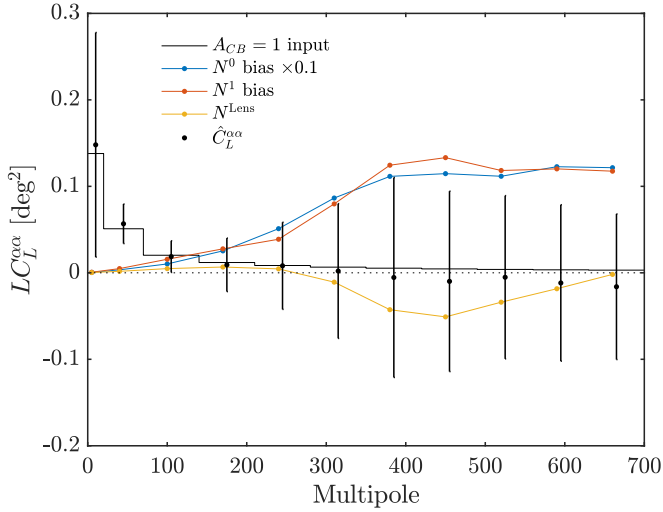
Figure 1. Example of the distortion field power spectra pipeline verification for the polarization rotation field $\alpha(\hat{n})$. The horizontal lines show the binned theory input for an $A_{CB} = 1$ spectrum. The $\hat{C}_L^{\alpha\alpha}$, the mean simulation bandpowers, matches the input spectrum after accounting for N^0, N^1, and the lensing bias N^{Lens}. The error bars show the standard deviation of the simulation realizations.

Q and U maps can be described as

$$[Q \pm iU](\hat{n}) = [\tilde{Q} \pm i\tilde{U}](\hat{n} + \nabla\Phi + \nabla \times \Omega), \qquad (2)$$

where the gradient $\nabla\Phi$ has the components $\partial_i\Phi$, and the curl $\nabla \times \Omega$ has the components $\epsilon_{ij}\partial_j\Omega$, where ϵ_{ij} is the antisymmetric symbol. To leading order, we obtain the map distortions

$$\delta[Q \pm iU](\hat{n}) = \nabla\Phi \cdot \nabla[\tilde{Q} \pm i\tilde{U}] \\ + \nabla \times \Omega \cdot \nabla[\tilde{Q} \pm i\tilde{U}](\hat{n}), \qquad (3)$$

which allow us to identify $\nabla \times \Omega$ and $\nabla\Phi$ with the curl and gradient mode of $\boldsymbol{p}(\hat{n})$, respectively. The gradient component of CMB lensing, Φ, is generated by the linear-order density perturbations, while the curl component, Ω, is only generated by second-order effects in scalar density perturbations or lensing by, for example, gravitational waves or cosmic strings (Dodelson et al. 2003; Cooray et al. 2005; Yamauchi et al. 2012). We expect these cosmological signals to be negligible (Hirata & Seljak 2003; Pratten & Lewis 2016; Fabbian et al. 2018).

The (gradient) CMB lensing potential power spectrum has been measured to high precision by many experiments using temperature, polarization, or both (Sherwin et al. 2017; Wu et al. 2019; Planck Collaboration et al. 2020a; Faúndez et al. 2020; Carron et al. 2022).

The distortion field $\tau(\hat{n})$ (amplitude modulation) can be generated by inhomogeneities in the reionization process, also referred to as patchy reionization. In addition to the kinematic Sunyaev–Zeldovich (kSZ) signal generated by the peculiar motion of ionized gas (Sunyaev & Zeldovich 1970, 1980), patchy reionization causes an uneven screening effect of photons (Dvorkin et al. 2009). The screening effect is described as

$$(Q \pm iU)(\hat{n}) = e^{-\tau_0(\hat{n})}(\tilde{Q} \pm i\tilde{U})(\hat{n}), \qquad (4)$$

$$\Rightarrow \delta(Q \pm iU)(\hat{n}) \approx -\tau_0(\hat{n})(\tilde{Q} \pm i\tilde{U})(\hat{n}), \qquad (5)$$

where $\tau_0(\hat{n})$ is the optical depth to recombination that varies for different line-of-sight directions $\hat{n}$. Taylor expanding

Equation (4), the screening effect from patchy reionization generates the distortion field $\tau(\hat{n})$.

The details of the patchy reionization process are still largely unknown. Recent searches for the redshifted 21 cm signal from neutral hydrogen by EDGES put a lower bound on the duration of reionization as $\Delta z \gtrsim 0.4$ (Monsalve et al. 2017). The kSZ power obtained from the South Pole Telescope (SPT) prefers $\Delta z \lesssim 4.1$ (Reichardt et al. 2021; Gorce et al. 2022). The constraints from Planck CMB temperature and polarization power spectra suggest that reionization occurred at $z_{\mathrm{re}} \approx 8$ with a duration of $\Delta z \lesssim 2.8$ (Planck Collaboration et al. 2016b). Previous work that studies patchy reionization through $\tau(\hat{n})$ reconstructions with CMB temperature and polarization include Gluscevic et al. (2013) and Namikawa (2018). We constrain the same crinkly surface model of patchy reionization where the power spectrum of the optical depth is given by

$$C_L^{\tau\tau} = \left(\frac{A^\tau}{10^4}\right)\frac{4\pi}{L_c^2}e^{-L^2/L_c^2}, \qquad (6)$$

with the amplitude A^τ and the coherence length L_c (Gluscevic et al. 2013).

The distortion field $\alpha(\hat{n})$ can be generated by a cosmic birefringence field that rotates the primordial $\tilde{Q}$ and $\tilde{U}$ according to

$$[Q \pm iU](\hat{n}) = e^{\pm 2i\alpha(\hat{n})}[\tilde{Q} \pm i\tilde{U}](\hat{n}), \qquad (7)$$

$$\Rightarrow \delta(Q \pm iU)(\hat{n}) \approx \pm i2\alpha(\hat{n})[\tilde{Q} \pm i\tilde{U}](\hat{n}). \qquad (8)$$

Two potential physical processes that can cause a rotation field $\alpha(\hat{n})$ are the coupling of CMB photons with pseudoscalar fields through the Chern–Simons term, also described as parity-violating physics, and Faraday rotation of the CMB photons due to interactions with background magnetic fields.

A massless axion-like pseudoscalar field a that couples to the standard electromagnetic term has the Lagrangian density (Carroll et al. 1990)

$$\mathcal{L} \supset \frac{g_{a\gamma}}{4}aF_{\mu\nu}\tilde{F}^{\mu\nu}, \qquad (9)$$

where $g_{a\gamma}$ is the coupling constant between the axion-like particles and photons, and $F_{\mu\nu}$ is the electromagnetic field tensor. The amount of rotation is given by

$$\alpha = \frac{g_{a\gamma}}{2}\Delta a. \qquad (10)$$

When the pseudoscalar field fluctuates in space and time, the change of the field integrated over the photon trajectory, Δa, varies across the sky and generates an anisotropic cosmic rotation field $\alpha(\hat{n})$. For a massless scalar field, the large-scale limit ($L \lesssim 100$) of the expected cosmic rotation power spectra is described by Caldwell et al. (2011),

$$\sqrt{\frac{L(L+1)C_L^{\alpha\alpha}}{2\pi}} = \frac{H_I g_{a\gamma}}{4\pi}, \qquad (11)$$

where H_I is the inflationary Hubble parameter.

A second physical process that could generate a cosmic rotation field $\alpha(\hat{n})$ is Faraday rotation of the CMB photons by primordial magnetic fields (PMFs). In the large-scale limit ($L \lesssim 100$), the cosmic rotation power spectra generated by a nearly scale-invariant PMF is (Yadav et al. 2012;

Table 1
The Fiducial Amplitude for the Scale-invariant Power Spectrum Used as Input for the Gaussian Simulations for the Calibration of the Normalization

D	τ	α	γ	f	d	q	p
$A_{\text{fid.}}^D$	10^{-3}	10^{-4}	10^{-6}	10^{-4}	10^{-10}	10^{-14}	10^{2}

De et al. 2013)

$$\sqrt{\frac{L(L+1)C_L^{\alpha\alpha}}{2\pi}} = 1.9 \times 10^{-4}\left(\frac{\nu}{150\text{GHz}}\right)^{-2}\left(\frac{B_{1\text{Mpc}}}{1\text{ nG}}\right), \quad (12)$$

where ν is the observed CMB frequency, and $B_{1\text{Mpc}}$ is the strength of the PMFs smoothed over 1 Mpc. The ν^{-2} frequency scaling of the Faraday rotation angle implies that a lower frequency offers better leverage for PMF measurement.

Observations from multiple CMB experiments have been employed to derive constraints on the anisotropies of the cosmic birefringence using $\alpha(\hat{n})$ reconstructions, which include the Wilkinson Microwave Anisotropy Probe (WMAP; Gluscevic et al. 2012), POLARBEAR (Ade et al. 2015), BK (BK–IX), Planck (Contreras et al. 2017; Gruppuso et al. 2020; Bortolami et al. 2022), the Atacama Cosmology Telescope (ACT; Namikawa et al. 2020), and the SPT (Bianchini et al. 2020).

3. Data and Simulations

In this paper, we use BK maps that use data up to and including the 2018 observing season, referred to as the BK18 maps. In particular, we focus on the two deepest maps: the 150 GHz map from BICEP2 and Keck Array data, which achieves 2.8 μK-arcmin over an effective area of around 400 deg^2, and the 95 GHz map from BICEP3, which achieves 2.8 μK-arcmin over an effective area of around 600 deg^2. These two data sets with the lowest noise levels are the most interesting for studying both the cosmological and instrumental effects related to the distortion fields.

We construct an apodization mask that downweights the noisier regions of the T, Q, and U maps. For the polarized Q and U maps, we use a smoothed inverse variance apodization mask similar to that used in BK–XIII. For the T map, we add a constant power of $10\,\mu$K^2 to the smoothed noise variance and invert it to construct the apodization mask. The mask is similar to a Wiener filter with flat weights in the central region dominated by sample variance and an inverse variance weight at the edges of the map. Additionally, for the analysis of T to P distortions, we mask the 20 point sources with the largest polarized fluxes from a preliminary SPT-3G catalog by applying a 0°.5 wide Gaussian divot at the location of each point source in the apodization mask. The effects of the point sources are discussed in Section 6.3 and Appendix E.

We reuse the standard sets of simulations described in BK–XIII and previous papers: lensed ΛCDM signal-only simulations constrained to the Planck T map (denoted by lensed-ΛCDM), sign-flip noise realizations, and Gaussian dust foreground simulations, each having 499 realizations. The details of the CMB signal and noise simulations are described in Section V of BK–I, and the dust simulations are described in Section IV.A of BICEP2/Keck & Planck Collaborations (2015) and Appendix E of Keck Array & BICEP2 Collaborations VI (2016). For estimating the noise bias of the distortion spectra constructed with TB estimators (described in

Section 4.3), an additional set of lensed CMB signal-only simulations with unconstrained temperatures are generated.

In addition to the standard simulation sets, we also generate simulations of random Gaussian realizations of the distortion fields, $D(\hat{n})$, that are characterized by certain power spectra. For pipeline verification and calibration of the normalization factors (Equation (22)), we use simulations described by a scale-invariant distortion spectrum,

$$\frac{L(L+1)}{2\pi}C_L^{DD} = A_{\text{fid.}}^D, \quad (13)$$

with fiducial amplitudes, $A_{\text{fid.}}^D$, and their specific values for each distortion field type given in Table 1.

For the amplitude modulation field $\tau(\hat{n})$, we generate Gaussian simulations of $\tau(\hat{n})$ according to the power spectrum in Equation (6). For comparing the sensitivity between quadratic estimators and BB power spectra for detecting distortion systematics, we generate Gaussian realizations of distortion fields with a scale-invariant spectrum within a narrow range of multipoles ($\Delta L = 50$).

The distortion field simulations and unconstrained temperature simulations are generated with the observation matrix $\mathcal{R}$ described in BK–VII. This matrix captures the entire mapmaking process, including the observing strategy, time-stream filtering, and deprojection of leading-order beam systematics. Simulations are rapidly generated with matrix multiplications,

$$\begin{pmatrix} Q^{\text{obs}} \\ U^{\text{obs}} \end{pmatrix} = \mathcal{R}\begin{pmatrix} Q^{\text{in}} \\ U^{\text{in}} \end{pmatrix} + \begin{pmatrix} Q^{\text{noise}} \\ U^{\text{noise}} \end{pmatrix}, \quad (14)$$

where Q^{in} and U^{in} are input signal maps, Q^{noise} and U^{noise} are sign-flip noise realizations, and Q^{obs} and U^{obs} are "as observed" output maps. Because of TE correlation in ΛCDM, such simulations are not fully accurate when the input T sky is not the same as that assumed in the construction of the deprojection operation that is built into the observing matrix.

4. Analysis of the Distortion Fields

4.1. Quadratic Estimator Construction

Since the BK-observed patch is relatively small (1%–2% of the total sky), we work in the flat-sky limit using Fourier transforms. A complex field, $D_1(\hat{n}) \pm iD_2(\hat{n})$, of spin s can be represented by its Fourier transform,

$$[D_a \pm iD_b]_L = (\pm 1)^s \int d\hat{n}[D_1(\hat{n}) \pm iD_2(\hat{n})]e^{\mp is\phi_L}e^{-i\bm{L}\cdot\hat{n}},$$

where $\phi_L = \cos^{-1}(\hat{n} \cdot \hat{\bm{L}})$. In particular, we note that τ, ω, and q are spin-0 fields; $p_1 \pm ip_2$ and $d_1 \pm id_2$ are spin-1 fields; $\gamma_1 \pm i\gamma_2$ are spin-2 fields; and $f_1 \pm if_2$ are spin-4 fields. We transform between even-parity modes D_a and odd-parity modes D_b and modes aligned with the R.A./decl. coordinate system of the underlying maps, D_1 and D_2, with a rotation

$$[D_a]_L = +[D_1]_L \cos(s\phi_L) + [D_2]_L \cos(s\phi_L), \quad (15)$$

$$[D_b]_L = -[D_1]_L \cos(s\phi_L) + [D_2]_L \cos(s\phi_L) \quad (16)$$

for fields with even-valued spin or

$$[D_a]_L = -i[D_1]_L \cos(s\phi_L) + i[D_2]_L \cos(s\phi_L), \quad (17)$$

$$[D_b]_L = +i[D_1]_L \cos(s\phi_L) + i[D_2]_L \cos(s\phi_L) \quad (18)$$

Table 2
Filter Functions $f_{l_1,l_2}^{D,XB}$ for the Different Distortion Field Estimators as Introduced in Equation (19)

D	f_{l_1,l_2}^{XB}
τ	$\tilde{C}_{l_1}^{XE} \sin 2(\phi_{l_1} - \phi_{l_2})$
α	$2\tilde{C}_{l_1}^{XE} \cos 2(\phi_{l_1} - \phi_{l_2})$
γ_a	$\tilde{C}_{l_1}^{TX} \sin 2(\phi_{L} - \phi_{l_2})$
γ_b	$\tilde{C}_{l_1}^{TX} \cos 2(\phi_{L} - \phi_{l_2})$
f_a	$\tilde{C}_{l_1}^{XE} \sin 2(2\phi_{L} - \phi_{l_1} - \phi_{l_2})$
f_b	$\tilde{C}_{l_1}^{XE} \cos 2(2\phi_{L} - \phi_{l_1} - \phi_{l_2})$
d_a	$\tilde{C}_{l_1}^{TX}(l_1\sigma) \cos 2(\phi_{L} + \phi_{l_1} - 2\phi_{l_2})$
d_b	$-\tilde{C}_{l_1}^{TX}(l_1\sigma) \sin 2(\phi_{L} + \phi_{l_1} - 2\phi_{l_2})$
q	$-\tilde{C}_{l_1}^{TX}(l_1\sigma)^2 \sin 2(\phi_{l_1} - \phi_{l_2})$
$p_a = \Omega$	$-\tilde{C}_{l_1}^{XE}\sigma(l_1 \times \hat{L}) \sin 2(\phi_{l_1} - \phi_{l_2})$
$p_b = \Phi$	$-\tilde{C}_{l_1}^{XE}\sigma(l_1 \cdot \hat{L}) \sin 2(\phi_{l_1} - \phi_{l_2})$

Note. Here X can be either T or B in order to obtain the filter functions for the TB or EB estimator, respectively. The $\tilde{C}_{l_1}^{TX}$ and $\tilde{C}_{l_1}^{XE}$ are lensed CMB power spectra corresponding to our fiducial model. Note that for the distortion fields p_a and p_b, we use the notation prevailing in CMB lensing, Ω and Φ.

for fields with odd-valued spin.

In Appendix A, we show that one can construct unbiased minimum variance TB and EB quadratic estimators for each distortion field given by

$$\bar{D}_L^{XB} = A_L^{D,XB} \int \frac{d^2l_1}{(2\pi)^2} X_{l_1} B_{l_2} \frac{f_{l_1,l_2}^{D,XB}}{C_{l_1}^{XX} C_{l_2}^{BB}}, \qquad (19)$$

$$\hat{D}_L^{XB} = \bar{D}_L^{XB} - \langle \bar{D}_L^{XB} \rangle, \qquad (20)$$

where $L = l_1 + l_2$, X may be T or E, and $C_{l_1}^{XX}, C_{l_2}^{BB}$ are the total observed power spectra including contributions from the noise and lensing. These estimators directly reconstruct the Fourier transform of the map distortions introduced in Equation (1), which are denoted by alphabetical subscripts a, b. The specific filter functions $f_{l_1,l_2}^{D,XB}$ for each distortion field D and estimator XB are listed in Table 2. Equation (20) shows the correction for the mean-field bias, which is estimated from simulations (Namikawa & Takahashi 2014a).

The analytical normalization factor is given by

$$A_L^{D,XB} = \left[\int \frac{d^2l_1}{(2\pi)^2} \frac{(f_{l_1,l_2}^{D,XB})^2}{C_{l_1}^{XX} C_{l_2}^{BB}} \right]^{-1}. \qquad (21)$$

In practice, we obtain the normalization factor empirically by running Monte Carlo simulations,

$$A_L^{D} = \frac{\langle |D_L^{in}|^2 \rangle}{\langle D_L^{in}(D_L^{sim})^* \rangle}, \qquad (22)$$

where D_L^{in} are the input distortion field Fourier modes, and D_L^{sim} are the unnormalized, reconstructed distortion modes. To obtain the input distortion Fourier modes D_L^{in}, the same apodization mask for the T, Q, and U maps is applied prior to the Fourier transform. We use the scale-invariant distortion input simulations (Equation (13)) to calibrate the normalization factor for all of the distortion fields except for lensing ($p(\hat{n})$ in Equation (1)), where the standard lensed-ΛCDM simulations are used.

We can construct TB estimators sensitive to the distortion fields only concerning polarization (τ, α, f_1, f_2, p) due to the nonzero TE correlation in the CMB. Therefore, all 11 distortion fields can be probed by both the EB and TB estimators with the weights listed in Table 2. However, the polarization-only distortion fields are better measured with the EB estimators, while the TB estimators have higher sensitivity to the distortion fields involving T to P leakage ($\gamma_{1/2}$, $d_{1/2}$, q).

4.2. Input E- and B-modes for Reconstruction

As described in BK–VII, the mixing of E- and B-modes due to map filtering and apodization is taken care of by the matrix-based purification method with purification matrices Π_B and Π_E. The purified E- and B-mode-only maps are

$$\begin{pmatrix} \hat{Q}^E \\ \hat{U}^E \end{pmatrix} = \Pi^E \begin{pmatrix} Q^{obs} \\ U^{obs} \end{pmatrix}, \qquad (23)$$

$$\begin{pmatrix} \hat{Q}^B \\ \hat{U}^B \end{pmatrix} = \Pi^B \begin{pmatrix} Q^{obs} \\ U^{obs} \end{pmatrix}, \qquad (24)$$

where Q^{obs} and U^{obs} can be either a simulation or the real map. The Fourier transform of the purified $\hat{Q}^{E/B}$ and $\hat{U}^{E/B}$ are used to construct the purified $\hat{E}$ and $\hat{B}$ modes, which are the input to the quadratic estimators.

Equation (19) minimizes the variance in the ideal case, ignoring beam smoothing, filtering, and apodization. In practice, transfer functions due to these effects must be compensated for in addition to E- and B-mode purification. In the observed BK maps, the $\hat{E}$ and $\hat{B}$ Fourier modes are corrected by

$$\bar{X}_l = t_{|l|}^X \hat{X}_l, \qquad (25)$$

$$t_l^X = \sqrt{\frac{C_l^{XX,in}}{C_l^{XX,out}}}, \qquad (26)$$

where $C_l^{XX,in}$ and $C_l^{XX,out}$ are the mean input and output spectra of the lensed-ΛCDM signal-only simulations, and t_l^X is the transfer function.

In practice, we find that using Fourier modes up to a multipole of 600 yields the best signal-to-noise ratio, whereas the $l = 600$–700 modes are noisy and can worsen the signal-to-noise ratio of the reconstruction due to a misestimation of t^X. Therefore, we use $l_{max} = 600$ as our baseline reconstruction parameter. To avoid potential contamination by dust, we mask out the lowest multipoles and use $l_{min}^B = 100$ for 95 GHz and $l_{min}^B = 150$ for 150 GHz. The l_{min}^B cutoff is chosen such that the observed dust B-mode power spectrum in the BK patch of sky is lower than the lensing B-mode power spectrum at $l > l_{min}^B$ using BK18 and Planck ΛCDM best-fit B-mode power spectra.

4.3. Estimating the Distortion Field Power Spectra

The power spectrum of a distortion field can be estimated by squaring the estimator $\hat{D}(L)$ from Equation (19),

$$\langle |\hat{D}_L|^2 \rangle = \hat{C}_L^{DD} + \hat{N}_L^{DD}, \qquad (27)$$

where $\hat{C}_L^{DD}$ is the observed distortion field power spectrum, and $\hat{N}_L^{DD}$ is the noise bias. When there is no distortion field present, the main contribution for $\hat{N}_L^{DD}$ is the disconnected N^0 bias,

which can be estimated by the realization-dependent method described in Namikawa et al. (2013) and BK–VIII,

$$\hat{N}_L^0 = \langle |\hat{D}_L^{E_1,\hat{B}} + \hat{D}_L^{\hat{E},B_1}|^2 \rangle_1$$
$$- \frac{1}{2} \langle |\hat{D}_L^{E_1,B_2} + \hat{D}_L^{E_2,B_1}|^2 \rangle_{1,2}, \qquad (28)$$

where $\hat{E}$ and $\hat{B}$ are the real E- and B-modes or a given simulation realization. The 499 simulation realizations are divided into two sets of roughly equal size, and the subscripts 1 and 2 stand for the first and second sets of simulations. The first term is averaged over the first set of simulations, while the second term is averaged over the first and second sets of simulations.

For the TB estimators that we use for systematics checks in Section 6, the realization-dependent bias is estimated in a similar manner to Equation (28) but with T instead of E. Since the standard lensed-ΛCDM simulations are generated with the temperature sky fixed to the Planck T map (see BK–I), an additional set of simulations with unconstrained T are used as the simulation sets 1 and 2 to be averaged over. The realization-dependent bias is evaluated for the observed $|\hat{D}_L^{\hat{T}\hat{B}}|^2$ and each of the reconstructed distortion bandpowers of the 499 standard constrained-T simulations. See Section 6.4 for more details.

When there is a distortion field signal, apart from the disconnected N^0 bias, there is an additional bias term that is proportional to the amplitude of the distortion field signal, referred to as the N^1 bias (Kesden et al. 2003). The N^1 bias can be estimated with two sets of simulations sharing the same distortion field realization (Story et al. 2015),

$$\hat{N}_L^1 = \langle |\hat{D}_L^{E_1,B_2} + \hat{D}_L^{E_2,B_1}|^2 \rangle_{1,2} - \langle \hat{N}_L^0 \rangle, \qquad (29)$$

where the subscripts 1,2 stand for the two sets of simulations with different CMB/noise realizations that share the same set of distortion field inputs, and $\langle \hat{N}_L^0 \rangle$ is the ensemble average of Equation (28).

Higher-order bias terms are either mitigated by our choice of weights (Hanson et al. 2011) or found to be small for our sensitivity levels (Böhm et al. 2018; Beck et al. 2018). Likewise, we do not expect a significant bias from galactic foregrounds in our polarization-based estimators (Beck et al. 2020) or from masking extragalactic sources in our temperature maps (Lembo et al. 2022).

Since the CMB signal contains gravitational lensing, the correlation between the lensing distortions and the various quadratic estimators can create a lensing bias N^{Lens}. This is estimated with the mean reconstructed distortion field spectrum $\langle C_L^{DD} \rangle$ of the lensed but otherwise undistorted ΛCDM simulations.

We verified that after the normalization from Equation (22) and accounting for N^0, N^1, and N^{Lens}, the input distortion spectra are recovered. Figure 1 shows as an example the polarization rotation $\hat{C}_L^{\alpha\alpha}$ spectra for a scale-invariant distortion input (Equation (13)) and its N^0, N^1, and N^{Lens} biases. Since the N^1 bias is proportional to the distortion field spectra, it is included as part of the signal when we constrain the amplitudes of cosmological models with the distortion field power spectra.

We measure the distortion field power spectrum in multipole bins with widths of $\Delta L = 70$, and the binned power spectrum values are referred to as bandpowers. The cosmological results in Section 5 are derived from $L \in [1,\ 350)$, since the

constraining power only comes from the low multipole modes, whereas in Section 6, we use $L \in [1,\ 700)$ to perform systematics checks. In certain applications where the lowest multipole modes are important, i.e., constraining cosmic birefringence models and performing distortion systematics tests, an additional $L \in [1,\ 20)$ bin is separated out from the $L \in [1,\ 70)$ bin.

4.4. Joint Analysis of Two Sets of Maps

When using the distortion fields as systematics checks, the two frequency maps are examined independently, since the BICEP3 (95 GHz) and BICEP2/Keck (150 GHz) maps may have different instrumental systematics. However, for studying cosmological signals, it is desirable to combine the results from the two frequencies into a single more powerful measurement. For the inference of cosmological information, we will only consider the most sensitive EB estimators in the combination of the two frequency maps.

Our approach is to form distortion field estimators with all possible combinations of the E- and B-modes, $\hat{D}^{E_1,B_1}$, $\hat{D}^{E_1,B_2}$, $\hat{D}^{E_2,B_1}$, and $\hat{D}^{E_2,B_2}$, where 1 and 2 stand for 95 and 150 GHz, respectively. In our analysis for the tensor-to-scalar ratio r (BK–I; BK–X; BK–XIII), we examine all possible auto- and cross-spectra from the multiple frequencies and experiments without forming a combined map. In this distortion field analysis, we follow a similar approach, where we construct all combinations of $\hat{D}^{E_i,B_j}$, combine their auto- and cross-spectra, and derive a joint cosmological constraint. While the cross-spectra approach might not necessarily yield the highest signal-to-noise ratio compared to an analysis of the combined map, the different combinations of spectra can provide consistency checks between data sets.

In Equation (27), the squares of the distortion field estimators are used to derive the auto-power spectra. Similarly, we take the four estimators $\hat{D}^{E_1,B_1}$, $\hat{D}^{E_1,B_2}$, $\hat{D}^{E_2,B_1}$, and $\hat{D}^{E_2,B_2}$ and compute all of the possible auto- and cross-spectra. With four individual distortion field estimates, we get a total of 10 spectra: four auto-spectra and six cross-spectra. Similarly to Equation (28), we compute the realization-dependent bias for the general scenario, including the case of the cross-spectra. The more general form of the realization-dependent N^0 bias with the two E maps W/Y and the two B maps X/Z is (Equation (A17) of Namikawa & Takahashi 2014a)

$$\hat{N}_L^0(\hat{W},\hat{X},\hat{Y},\hat{Z}) = \langle -|\hat{D}^{W_1,X_2}\hat{D}^{*Y_2,Z_1}|^2$$
$$+ |\hat{D}^{W_1,\hat{X}}\hat{D}^{*Y_1,\hat{Z}}|^2 + |\hat{D}^{W_1,\hat{X}}\hat{D}^{*\hat{Y},Z_1}|^2$$
$$+ |\hat{D}^{\hat{W},X_1}\hat{D}^{*Y_1,\hat{Z}}|^2 + |\hat{D}^{\hat{W},X_1}\hat{D}^{*\hat{Y},Z_1}|^2$$
$$- |\hat{D}^{W_1,X_2}\hat{D}^{*Y_1,Z_2}|^2 \rangle_{1,2}, \qquad (30)$$

where the subscripts 1,2 represent the two sets of simulations with different CMB/noise realizations, and D^* is the complex conjugate of D. Here $\hat{W}$, $\hat{Y}$ can be either the observed 95 or 150 GHz E-modes, and $\hat{X}$, $\hat{Z}$ can be either the observed 95 or 150 GHz B-modes. It can be verified that Equation (30) reduces to Equation (28) when all four maps W, X, Y, and Z come from the same frequency map.

The 10 possible auto- and cross-spectra are combined linearly with appropriate weights so that the variance of the

combined bandpowers is minimized,

$$C_b = \sum_i w_{b,i} C_{b,i}, \qquad (31)$$

where i stands for the 10 spectral indices, b stands for the bins of the bandpowers, and the weights $w_{b,i}$ are a function of both the bins and the spectral indices. The weights are

$$w_{b,i} = \frac{\mathrm{mean}_k(\bar{C}_{b,k}) \sum_j \mathrm{Cov}_{b,ij}^{-1} \bar{C}_{b,j}}{\sum_{jk} \bar{C}_{b,j} \mathrm{Cov}_{b,jk}^{-1} \bar{C}_{b,k}}, \qquad (32)$$

where $\bar{C}_{b,i}$ is the mean power from the 499 simulations of spectrum i and bin b, and $\mathrm{Cov}_{b,ij}^{-1}$ is the covariance matrix of the bandpowers of bin b from the 10 spectra. The minimum variance bandpowers C_b from Equation (31) combine the statistical power from the two frequency maps and are used to constrain the corresponding cosmological processes.

5. Results: Cosmology from Distortion Fields

In the following subsections, we present the observed distortion field spectra and the derived cosmological constraints from $\Phi(\hat{\boldsymbol{n}})$, $\tau(\hat{\boldsymbol{n}})$, and $\alpha(\hat{\boldsymbol{n}})$ corresponding to gravitational lensing, patchy reionization, and cosmic birefringence.

5.1. Gravitational Lensing

In Table 2, the weights for reconstructing the gradient, Φ, and curl component, Ω, are listed. We use the gradient part to constrain the amplitude of the lensing signal parameterized as $A_L^{\phi\phi}$ while using the curl part as a systematics check in Section 6.

It is often more convenient to work with the lensing-mass (convergence) field κ, since the lensing potential has a red spectrum, while the lensing-mass field has a nearly flat spectrum (Planck Collaboration et al. 2016a). The lensing convergence κ is related to the lensing potential Φ as

$$\kappa = -\frac{1}{2}\nabla^2\Phi. \qquad (33)$$

For the Fourier transform, we have

$$\kappa_{\boldsymbol{L}} = \frac{L(L+1)}{2}\Phi_{\boldsymbol{L}}, \qquad (34)$$

where $L = |\boldsymbol{L}|$. Similarly, we also define the analogous quantity for the lensing rotation ω as

$$\omega_{\boldsymbol{L}} = \frac{L(L+1)}{2}\Omega_{\boldsymbol{L}}. \qquad (35)$$

In Equation (22), where we empirically calibrate the normalization factor, we correlate the input distortion field with the reconstruction. Before performing the Fourier transform and cross-correlation, the inverse variance apodization masks are applied to the input distortion fields. Because the κ spectrum is relatively flat compared to the red Φ spectrum, it is better to apply the apodization mask to the κ map instead of the Φ map to avoid mode mixing (BK–VIII):

$$\Phi_{\boldsymbol{L}} = \frac{2}{L^2}\int d^2\hat{\boldsymbol{n}} e^{-i\hat{\boldsymbol{n}}\cdot\boldsymbol{L}}\kappa(\hat{\boldsymbol{n}}). \qquad (36)$$

The 10 possible auto- and cross-spectra for the lensing reconstruction are shown in Figure 2, where the lensing convergence spectrum $C_L^{\kappa\kappa} \approx 4/L^4 C_L^{\Phi\Phi}$ is plotted. The four diagonal subplots are the auto-spectra from the four possible Φ^{E_i,B_j}, while the other six are from cross-correlating the different Φ^{E_i,B_j}. The top left subplot is derived from only 95 GHz, and the bottom right subplot is derived from only 150 GHz. The other eight subplots combine some information from both 95 and 150 GHz.

In Figure 3, we show the reconstructed $\hat{C}_L^{\kappa\kappa}$ of 95 GHz only, 150 GHz only, and all 10 spectra combined. With the bandpowers in Figure 3, we fit for the amplitude of the lensing potential power spectrum by taking a weighted mean of the real bandpowers over the fiducial simulation bandpowers (BK–VIII). With a linear model $\hat{C}_b = A_L^{\phi\phi} C_b^f$ of the noise-debiased power spectrum, where C_b^f is the fiducial model corresponding to the Planck ΛCDM prediction from their 2013 release[21] (Planck Collaboration et al. 2014), the least-squares fit for $A_L^{\phi\phi}$ is

$$A_L^{\phi\phi} = \frac{\sum_{bb'} \hat{C}_b \mathrm{Cov}_{bb'}^{-1} C_{b'}^f}{\sum_{bb'} C_b^f \mathrm{Cov}_{bb'}^{-1} C_{b'}^f}, \qquad (37)$$

where $\hat{C}_b = \hat{C}_L^{\kappa\kappa}$ is the observed lensing convergence bandpower, C_b^f is the mean bandpower from the lensed-ΛCDM simulations, and $\mathrm{Cov}_{bb'}$ is the bandpower covariance matrix from the same lensed-ΛCDM simulations.

The best-fit $A_L^{\phi\phi}$ are

$$A_L^{\phi\phi} = 0.89 \pm 0.23, \quad \text{for 95 GHz only}, \qquad (38)$$

$$A_L^{\phi\phi} = 1.05 \pm 0.33, \quad \text{for 150 GHz only}, \qquad (39)$$

$$A_L^{\phi\phi} = 0.95 \pm 0.20, \quad \text{for 10 spectra combined.} \qquad (40)$$

Since the lensing reconstruction is close to sample variance limited in the central parts of the map, the larger map coverage from BICEP3 95 GHz produces a tighter $\sigma(A_L^{\phi\phi}) = 0.23$ compared to the 150 GHz $\sigma(A_L^{\phi\phi}) = 0.33$. When all of the cross-spectra between the two frequencies are combined, we achieve $\sigma(A_L^{\phi\phi}) = 0.20$, an $\approx 15\%$ reduction compared to 95 GHz only. This is around a factor of 2 improvement from the previous BK–VIII result of $A_L^{\phi\phi} = 1.15 \pm 0.36$. However, note that the lensing amplitude is better constrained by the B-mode power spectrum with $A_L^{BB} = 1.03_{-0.09}^{+0.08}$ in BK–XIII. We compile these constraints on the lensing amplitude in Figure 4.

5.2. Patchy Reionization

Following Gluscevic et al. (2013) and Namikawa (2018), we use the $\tau(\hat{\boldsymbol{n}})$ reconstruction from the EB estimator to constrain a simple crinkly surface model. The model describes a scenario in which the universe suddenly goes from neutral to ionized but with a reionization surface that is crinkled on a comoving scale of $R_c \approx 200\,\mathrm{Mpc}\,(L_c/150)^{-1}$. The predicted power spectrum in Equation (6) consists of white noise smoothed on an angular scale of $\theta_C = \pi/L_c$. Fiducial model spectra are shown in Figure 5 for $L_c = 100$, 200, 400, and 800. The use of this parameter space is only valid in the assumption of this simplified model, as it assumes an instantaneous reionization.

---

[21] The lensing B-mode power from the Planck 2013 parameters is around 5% higher than the Planck 2018 results (Planck Collaboration et al. 2021). This difference is small compared to the uncertainties in the present work.
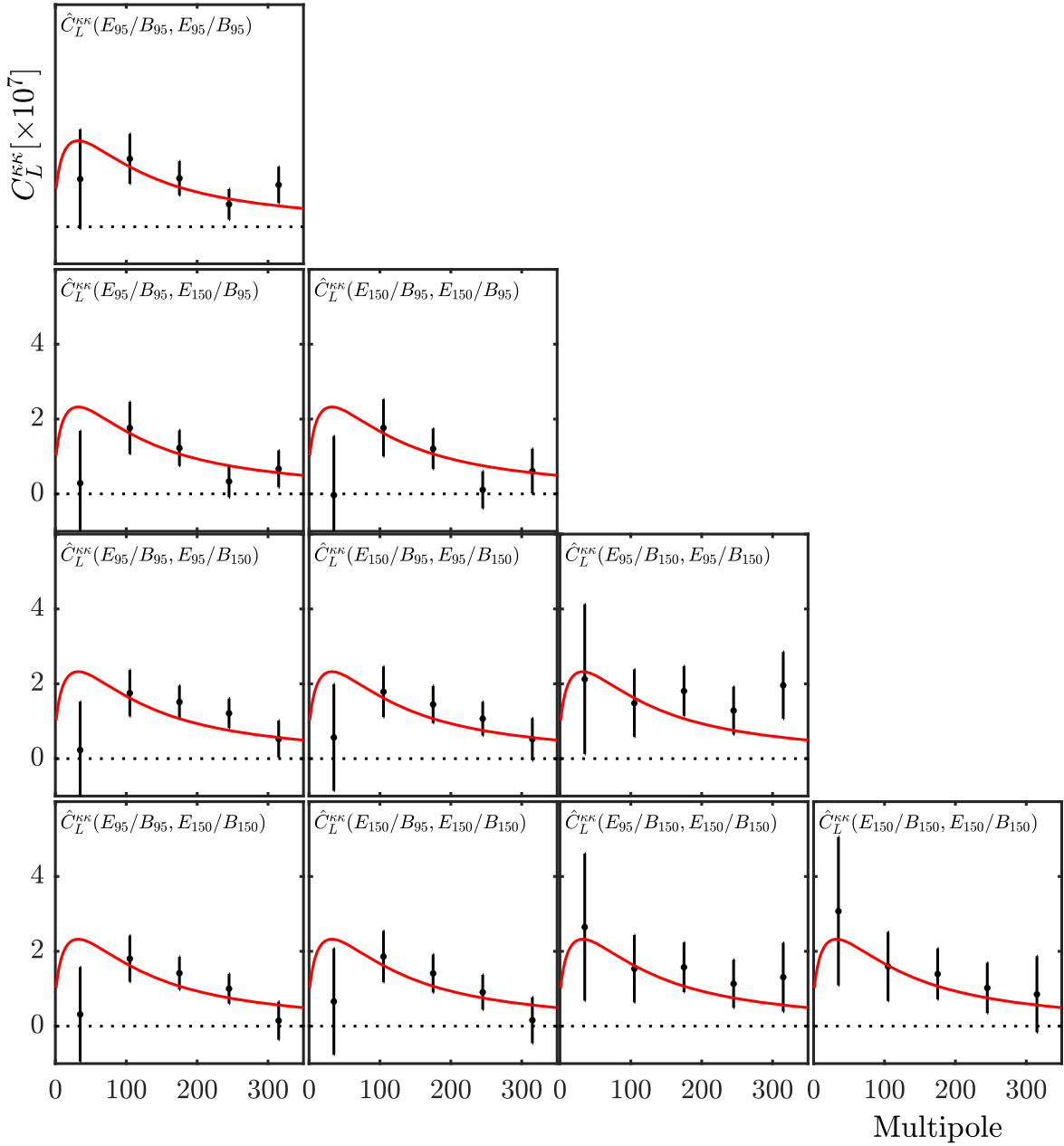
Figure 2. The 10 different ways to combine two sets of E and B maps to form the lensing convergence spectrum estimator $\hat{C}_L^{\kappa\kappa}$. The red line is the theoretical lensing convergence spectrum corresponding to our fiducial model assuming Planck 2013 cosmological parameters (Planck Collaboration et al. 2014). The top left subplot is the auto-spectrum from 95 GHz, while the bottom right subplot is the auto-spectrum from 150 GHz. The other subplots contain information from both 95 and 150 GHz. We examine the 10 spectra individually, all 10 spectra combined, and some other data combinations and find that they are all consistent with the lensed-ΛCDM predictions.

As such, the parameter L_c has no physical meaning, and limitations can be evaded with a more realistic model of the reionization history.

The amplitude A^τ is constrained with a log likelihood based on Hamimeche & Lewis (2008),

$$-2\ln L(A^\tau) = \sum_{bb'} g(\hat{R}_b) C_b^f \text{Cov}_{bb'}^{-1} C_{b'}^f g(\hat{R}_{b'}), \qquad (41)$$

where C_b^f are the mean bandpowers from the simulations of the fiducial model, $g(x) = \text{sign}(x - 1)\sqrt{2(x - \ln x - 1)}$, and $\hat{R}_b$ is the per-bin ratio of the observed bandpowers over the fiducial bandpowers including the N^0, N^1, and lensing bias

N^{Lens}:

$$\hat{R}_b = \frac{\hat{C}_b^{\tau\tau} + N_b^0 + N_b^{\text{Lens}}}{A^\tau(C_b^f + N_b^1) + N_b^0 + N_b^{\text{Lens}}}. \qquad (42)$$

Using the method outlined in Section 4.4, Figure 5 shows the reconstructed $\hat{C}_L^{\tau\tau}$ for 150 GHz auto-spectra, 95 GHz auto-spectra, and all 10 auto- and cross-spectra combined. We see that the BK data are consistent with zero, offering no evidence for a patchy reionization signal, consistent with earlier limits derived from WMAP and Planck temperature maps (Gluscevic et al. 2013; Namikawa 2018).

We proceed to set upper limits on A^τ in Equation (6) using the log likelihood of Equation (41). Fiducial simulations of L_c
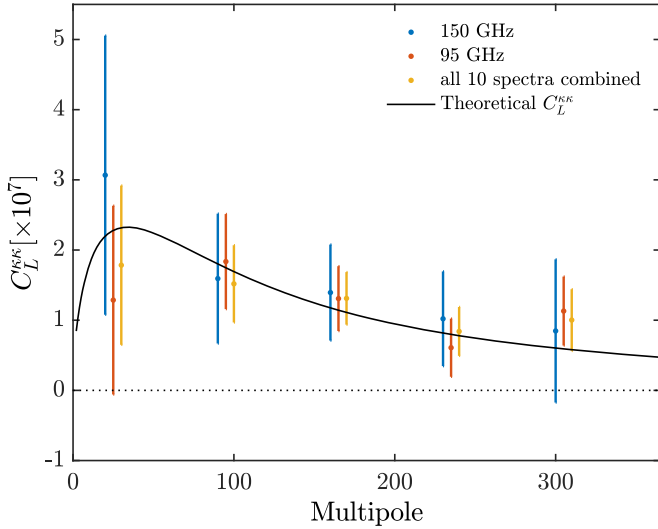
Figure 3. Lensing convergence power spectrum $C_L^{\kappa\kappa}$ for the 95 GHz auto-spectrum, the 150 GHz auto-spectrum, and all 10 auto- and cross-spectra combined.

Figure 4. Comparison of the constraints of this paper with the latest constraints of the lensing amplitude A_L from the Planck PR3 temperature power spectrum, TT+lowE (Planck Collaboration et al. 2020b); the Planck PR4 lensing reconstruction (Carron et al. 2022); the BK18 B-mode power spectrum measurement (BK–XIII) using the same data set; and the previous measurement from the lensing potential reconstruction using BK14 data (BK–VIII). Bullet points denote constraints from the lensing potential auto-power spectrum, and squares are used for measurements using CMB two-point functions.

Figure 5. Data and model power spectra of patchy reionization. The solid lines show fiducial model spectra from Equation (6) for $L_c = 100$, 200, 400, and 800. The data points show $\hat{C}_L^{\tau\tau}$ for 150 GHz only, 95 GHz only, and all 10 spectra combined.

Figure 6. Constraints on the amplitude $A^\tau(L_c)$ of Equation (6) obtained from this work (green) and in the previous work (Gluscevic et al. 2013; Namikawa 2018). The colored regions are excluded.

at 100, 200, 400, and 800 are used to derive the constraints. In Table 3, the 2σ (95% C.L.) upper limits on A^τ for 95 GHz only, 150 GHz only, and all 10 spectra combined are listed. The sensitivity primarily comes from the 95 GHz map.

Following Gluscevic et al. (2013) and Namikawa (2018), we plot the constraints of Table 3 in the A^τ versus L_c parameter space. In Figure 6, the constraint derived from our data is seen to be between the constraints from WMAP TT and Planck TT. The noise level of the $\hat{\tau}$ reconstruction in the BICEP patch is roughly the same as the reconstruction from the Planck TT estimator. However, Planck's wider sky coverage significantly reduces the overall sample variance. According to Gluscevic et al. (2013), the lower limit on the duration of reionization $\Delta z \gtrsim 0.4$ obtained by EDGES (Monsalve et al. 2017) can be translated to $A^\tau \gtrsim 0.1$, so only a narrow allowed band remains.

5.3. Cosmic Birefringence

The two physical processes that can lead to anisotropic cosmic birefringence, parity-violating physics and PMFs,

Table 3
The 2σ Upper Limits for $A^\tau(L_c)$ Derived from the 95 GHz Auto-spectrum, the 150 GHz Auto-spectrum, and All 10 Spectra Combined

	2σ Upper Limit on A^τ		
L_c	150 GHz	95 GHz	All 10 Spectra
100	76	24	19
200	51	17	16
400	72	27	26
800	190	77	71

Note. The corresponding $\hat{C}_L^{\tau\tau}$ is shown in Figure 5, and the fiducial model spectrum is Equation (6).

produce the predicted power spectra given in Equations (11) and (12). These are both of the form $L(L + 1)C_L^{\alpha\alpha} = $ constant. Following previous conventions (BK–IX; Bianchini et al. 2020; Namikawa et al. 2020), we parameterize the power
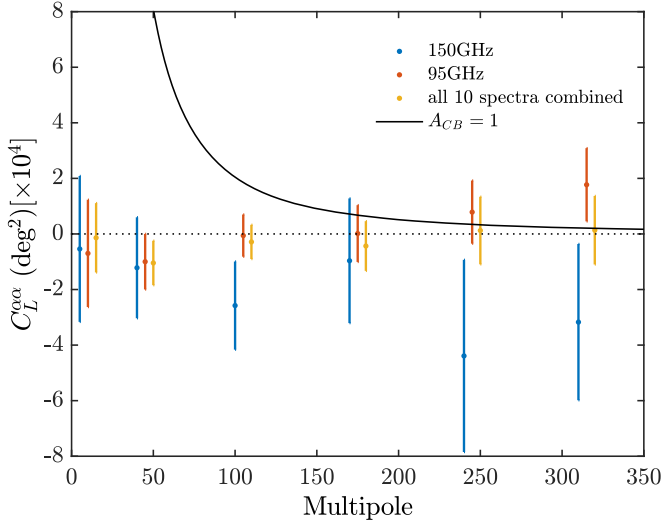
Figure 7. Cosmic birefringence power spectra $\hat{C}_L^{\alpha\alpha}$ for 95 GHz only, 150 GHz only, and all 10 spectra combined. The black line is the fiducial spectra from Equation (43) with $A_{CB} = 1$. Compared to Figures 3 and 5, one additional bin of $L \in [1, 20]$ is separated out from the $L \in [1, 70]$ bin, since the lowest multipoles are important for constraining A_{CB}.

spectra with A_{CB},

$$\frac{L(L+1)C_L^{\alpha\alpha}}{2\pi} = A_{CB} \times 10^{-4} \; [\text{rad}^2]. \tag{43}$$

In standard BK analysis, the overall polarization angle is adjusted to minimize the observed TB and EB power spectra. After this self-calibration, the polarization maps lose sensitivity to a uniform polarization rotation but are still sensitive to anisotropic rotations.

5.3.1. Constraints on Parity-violating Physics

The best constraints from our data set on the coupling constant $g_{a\gamma}$ between axion-like particles and photons (Equation (11)) are derived using the combined minimum variance $\hat{C}_L^{\alpha\alpha}$ of the two frequency maps. Following the method outlined in Section 4.4, the reconstructed $\hat{C}_L^{\alpha\alpha}$ for 95 GHz, 150 GHz, and all 10 spectra combined are shown in Figure 7.

The $\hat{C}_L^{\alpha\alpha}$ in Figure 7 are consistent with the unrotated lensed-ΛCDM+dust+noise simulations. In a similar approach to Namikawa et al. (2020) and Bianchini et al. (2020), we use a log likelihood based on Hamimeche & Lewis (2008) to evaluate the 95% 2σ upper limit for A_{CB}. This likelihood is the same as Equations (41) and (42) but with A_{CB} in place of A^τ. We obtain a 95% confidence upper limit of $A_{CB} \leqslant 0.044$. Using Equation (11), this corresponds to an upper limit on the coupling constant $g_{a\gamma}$,

$$g_{a\gamma} \leqslant \frac{2.6 \times 10^{-2}}{H_I}. \tag{44}$$

This is a factor of 3 improvement over our previous results using the BK14 maps in BK–IX: $g_{a\gamma} \leqslant 7.2 \times 10^{-2}/H_I$. It is also somewhat better than the constraints from ACT, $g_{a\gamma} \leqslant 4 \times 10^{-2}/H_I$ (Namikawa et al. 2020), and SPT, $g_{a\gamma} \leqslant 4 \times 10^{-2}/H_I$ (Bianchini et al. 2020).
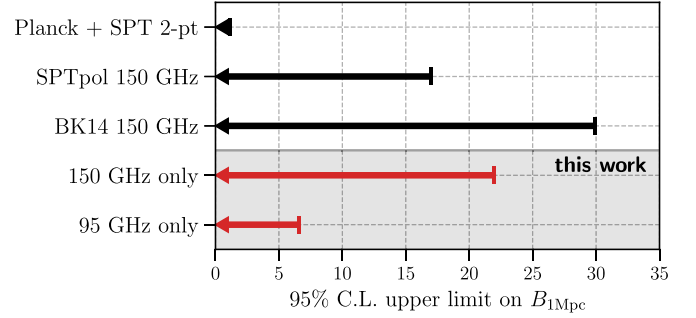
Figure 8. Comparing the constraint on the strength of PMFs smoothed over 1 Mpc, $B_{1\text{Mpc}}$, of this work with constraints from SPTpol anisotropic birefringence reconstruction (Bianchini et al. 2020) and Planck and SPTpol CMB power spectra (Zucca et al. 2017).

5.3.2. Constraints on PMFs

To derive constraints on PMFs, we study the two frequency maps separately, since the polarization angle rotation from Faraday rotation scales with frequency as ν^{-2} (Equation (12)). With the 95 GHz only and 150 GHz only spectra shown in Figure 7, we again use the log likelihood Equation (41) to derive 95% upper limits on A_{CB}, where we obtain $A_{CB} \leqslant 0.097$ for 95 GHz and $A_{CB} \leqslant 0.17$ for 150 GHz. With Equation (12), we convert these constraints on A_{CB} to the following constraints on PMFs $B_{1\text{Mpc}}$:

$$B_{1\text{Mpc}} \leqslant 6.6 \text{ nG}, \quad \text{for 95 GHz}, \tag{45}$$

$$B_{1\text{Mpc}} \leqslant 22 \text{ nG}, \quad \text{for 150 GHz}. \tag{46}$$

We show that the previously published constraints from CMB four-point function measurements in Figure 8, which are derived from 150 GHz maps, are SPT, $B_{1\text{Mpc}} \leqslant 17$ nG (Bianchini et al. 2020), and BK–IX, $B_{1\text{Mpc}} \leqslant 30$ nG. The leading constraint on this parameter is $B_{1\text{Mpc}} \leqslant 1.2$ nG for a nearly scale-invariant PMF, derived from a combination of Planck and SPT two-point power spectra (Zucca et al. 2017). Through the effect of PMFs on the postrecombination ionization history, Paoletti et al. (2022) were able to constrain the amplitude of the magnetic fields to $\sqrt{B^2} < 0.69$ nG.

The A_{CB} constraint derived from BICEP3 95 GHz alone ($A_{CB} \leqslant 0.097$) is comparable to the upper limits from SPT and ACT, but the resulting constraint on $B_{1\text{Mpc}}$ is considerably better because of the advantage of the lower-frequency leverage with the ν^{-2} scaling.

5.4. Consistency Checks and Null Tests

In this subsection, we discuss consistency checks and jackknife null tests for the three distortion fields $\tau(\hat{\boldsymbol{n}})$, $\alpha(\hat{\boldsymbol{n}})$, $\kappa(\hat{\boldsymbol{n}})$ that have been used to derive science constraints. We want to emphasize that the BK18 data set has passed a comprehensive set of data validations (BK–I; BK–III; BK–XIII), most importantly, the jackknife null tests on the EE/BB power spectra. In the next section (Section 6), we study all of the distortion effects in Equation (1) as systematics checks, providing further evidence that the BK18 data set has systematic effects controlled below the level of statistical uncertainty. In this subsection, we focus on demonstrating the robustness of the reconstructed distortion field spectra with different analysis choices and present some additional null tests for the three distortion fields being used to derive science results.

5.4.1. Consistency Checks

As consistency checks of the $\kappa(\hat{\boldsymbol{n}})$, $\tau(\hat{\boldsymbol{n}})$, and $\alpha(\hat{\boldsymbol{n}})$ reconstructions, the distortion bandpowers are constructed while altering some choices of the analysis. We summarize the conclusions here and provide detailed PTE values in Appendix C.

1. Input E-/B-mode multipoles.

   Similarly to BK–VIII and BK–IX, we lower the maximum multipole ℓ_{max} from 600 to 400, raise the minimum multipole ℓ_{min} to 200, or lower the B-mode maximum multipole ℓ_{max}^{B} from 600 to 350. The results from these three alternate choices are all consistent with the lensed-ΛCDM+dust+noise simulations. Additionally, the shift of the observed bandpowers from the three alternate choices versus the baseline are also consistent with the shift in the simulation bandpowers for both 95 and 150 GHz and all three fields α, τ, and κ.

2. Differential beam ellipticity.

   In BK analysis, the T to P leakage from differential gain and pointing is filtered out with the technique we call deprojection (BK–III). However, the T to P leakage from differential beam ellipticity cannot be treated with a direct filtering operation because the CMB TE correlation would cause a bias. Instead, we subtract a leakage template derived from the measured differential beam map ellipticity. We repeat the analysis without the subtraction and find very small changes in the reconstructed spectra, similar to what has been seen by Mirmelstein et al. (2021).

3. Alternate foreground models.

   In Appendix D, the different foreground models explored in the main BK18 analysis (BK–XIII) are used instead of the Gaussian dust simulations. We find that with the realization-dependent method and the baseline choice of $\ell_{min}^{B} = 100/150$ for 95 and 150 GHz, the shifts in the bandpowers when switching to the alternate foreground models, or to no foreground, are negligible.

5.4.2. Effects of Absolute Calibration Error

Although the distortion fields $\kappa(\hat{\boldsymbol{n}})$, $\tau(\hat{\boldsymbol{n}})$, and $\alpha(\hat{\boldsymbol{n}})$ are dimensionless quantities, the EB quadratic estimator construction will lead to a distortion spectrum C_L^{DD} that depends on the overall amplitude of the polarization map. An absolute calibration uncertainty of δ on the polarization map will translate to a systematic uncertainty of 4δ on either the A_{CB}/A^{τ} upper limits or the amplitude of the lensing potential $A_L^{\phi\phi}$ (BK–VIII). The absolute calibration procedure that correlates the observed T with the Planck T map (BK–I) is estimated to have an uncertainty of 0.3%. The polarization efficiency is high ($\approx$99%), with an uncertainty of $\lesssim$0.5% (BK–I; BK–II). Therefore, we estimate that the systematic uncertainty on $A_L^{\phi\phi}$ from the absolute calibration of the polarized map is around $4\delta \lesssim 3\%$.

5.4.3. Jackknife Null Tests

We perform distortion field reconstruction on the 14 flavors of differenced (jackknife) maps that are designed to target different systematics in the main line analysis (BK–I; BK–III; BK–X; BK–XIII). The distortion field reconstruction is done with the full E-modes and jackknife B-modes, written as

$\hat{D}^{E_{full}, B_{jack}}$. We are interested in probing systematic effects that can potentially bias the distortion field reconstructions. For our B-mode search in the main analysis, we are most worried about E-to-B leakage terms. Further, B-mode systematics that can be interpreted as a distortion field coupled with the full E-modes would be the most concerning contamination in terms of biasing the distortion field science results. Hence, we focus on the particular combination of $\hat{D}^{E_{full}, B_{jack}}$ as opposed to $\hat{D}^{E_{jack}, B_{full}}$. While the latter would be more sensitive if Equation (1) were a perfect model of our instrumental systematic contamination and systematic effects acted symmetrically on E- and B-modes, we decide to perform a more focused search of E-to-B leakage terms with the $\hat{D}^{E_{full}, B_{jack}}$ estimator.

With the method outlined in Section 4.3, we reconstruct the observed $\hat{C}_L^{DD}$ from $\hat{D}^{E_{full}, B_{jack}}$ and compare it to C_L^{DD} from the 499 lensed-ΛCDM+dust+noise simulations by evaluating the χ and χ^2 values,

$$\chi^2 = \sum_{bb'} (\hat{C}_b - \langle C_b \rangle) \text{Cov}_{bb'}^{-1} (\hat{C}_{b'} - \langle C_{b'} \rangle), \qquad (47)$$

$$\chi = \sum_b (\hat{C}_b - \langle C_b \rangle)/\sigma(C_b), \qquad (48)$$

where $\text{Cov}_{bb'}$ is the bandpower covariance matrix from 499 simulations, $\hat{C}_b$ is the observed distortion field bandpower, and $\langle C_b \rangle$ is the mean bandpower from the simulations. We also compute the χ and χ^2 values for each of the 499 simulation realizations and evaluate the probability to exceed (PTE) or p-value by counting the percentage of simulations that have larger χ or χ^2.

There are 14 (jackknives) $\times$ 3 (fields) $\times$ 2 (frequency maps) = 84 PTE values for both χ and χ^2 statistics. These values are histogrammed in Figure 9. The value for the χ PTE closest to zero or unity is 0.006, and the lowest χ^2 PTE is 0.008. Taking into account the look-elsewhere effect, we can construct a global statistical test that compares these real data values to the simulations. The specific procedure is as follows:

$$\chi^2 \text{ extreme PTE: } p_{\chi^2} = \min_p(p), \qquad (49)$$

$$\chi \text{ extreme PTE: } p_{\chi} = \min_p (\min(p, 1-p)), \qquad (50)$$

$$\text{overall extreme PTE: } p_{all} = \min(p_{\chi}, p_{\chi^2}), \qquad (51)$$

where p in Equation (49) are the 84 χ^2 PTE values, and p in Equation (50) are the 84 χ PTE values for the real data or a given simulation realization. The quantities p_{χ^2} and p_{χ} are the most extreme χ^2 and χ PTEs, and the overall most extreme PTE p_{all} is the smaller of p_{χ} and p_{χ^2}.

We find that the most extreme value for the real bandpowers is $p_{all}^{obs} = 0.006$. Comparing p_{all} between the observation and simulations, the probability of getting a value smaller than the observed value is 0.59. Therefore, we conclude that there is no evidence of spurious B-modes in the $\kappa(\hat{\boldsymbol{n}})$, $\tau(\hat{\boldsymbol{n}})$, and $\alpha(\hat{\boldsymbol{n}})$ reconstructions from the jackknife maps.

6. Results: Distortion Fields as Systematics Tests

In this section, we comprehensively investigate the distortion fields potentially caused by systematics and consider different types of instrumental effects that could produce these distortions. In the main line analysis for the tensor-to-scalar ratio r (BK–I; BK–VI; BK–X; BK–XIII) the most fundamental
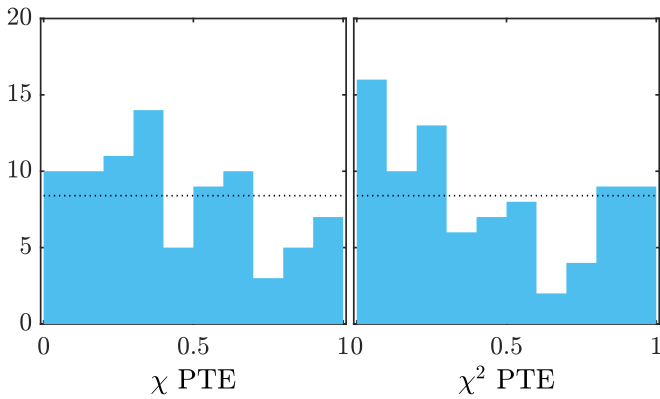
Figure 9. Distributions of the 84 χ/χ^2 PTE values from 14 jackknives and three distortion fields of two real data frequency maps.

guards against systematics are the map jackknife (or null) tests. Maps are made by splitting the data into (approximate) halves according to criteria that would be expected to result in a nearly equal signal but potentially different systematic contamination. The split maps are then differenced, and the EE, BB, and EB spectra of the result are compared to simulations of signal plus noise. Well-chosen jackknife splits can amplify systematics that cancel in the full coadd map (BK–III). It must be emphasized again that the published BK measurements of the tensor-to-scalar ratio, including the latest BK18 release, have passed all of these null tests.

However, systematics detection and mitigation based on the distortion fields may complement and enhance the standard map jackknife tests in several ways. When using line-of-sight distortion fields for systematics, we are checking for spurious B-modes in the full Q/U maps. Therefore, any spurious B-modes detected will indeed be present in the data set used to derive the science results. There are systematics that naturally cancel out with many detectors or with the instrument boresight rotation of the observation strategy (BK–III, Sections 2.3 and 4). In this case, failing a jackknife test might not necessarily mean that there was significant contamination in the full coadd maps. Conversely, there could hypothetically be systematic contamination in the full coadd map that somehow cancels in all considered jackknife splits.

In addition, going beyond the two-point statistics offers more information about the observed maps. Each of the distortion fields corresponds to a certain type of systematics. Therefore, failing the systematics check for a certain distortion field can offer hints as to where to investigate. Furthermore, we will show that the quadratic estimators for distortion fields are usually more sensitive compared to the BB spectrum at detecting the corresponding distortions. Any spurious B-modes from distortion fields would be detected by their quadratic estimators before they significantly affect the BB spectrum.

In the mapmaking process, the Q and U modes that are potentially contaminated through beam systematics, in particular differential gain and pointing, are filtered out by the deprojection procedure (BK–I). The choice of deprojection timescale of around 10 hr is a compromise; a shorter deprojection timescale guards against systematics that vary over short periods but at the same time removes more modes and reduces the overall statistical power (BK–I; BK–III). The distortion fields γ_1, γ_2 are sensitive to the modes corresponding to the differential gain, while d_1, d_2 are sensitive to the modes corresponding to differential pointing. Therefore, the distortion

field estimators as systematics checks can guard against beam systematics that vary faster than the 10 hr deprojection timescale, eluding deprojection.

However, there are many classes of systematic contamination that do not correspond to any of the distortion fields. Therefore, the distortion field systematics tests should be treated as a useful complementary check for the standard jackknife tests, rather than a replacement.

For different experiments with different ways of measuring CMB polarization (e.g., pair differencing versus rotating half-wave plate), the mapping between detector systematics to the final line-of-sight distortion field can vary. We will discuss the case for experiments similar to BK that take the pair difference signal from pairs of detectors with orthogonal polarization directions and then use boresight angle rotation to get a distribution of polarization angles to be able to solve for Q/U (BK–II). Hu et al. (2003) offered a more general discussion of the connection between instrumental systematics and distortion fields.

6.1. Instrumental Systematics and Distortion Fields

Since the telescope is constantly scanning the sky, a time-varying spurious systematic effect will translate into a position-dependent error in the map, which can be associated with different distortions (Hu et al. 2003; Yadav et al. 2010). On the other hand, a spurious systematic effect that stays constant in time but varies from detector to detector will also cause a position-dependent error in the map, since different detectors cover different regions of the map.

Miscalibration of detector gains (pair sum timestream signal) would be captured in the amplitude modulation field $\tau(\hat{n})$. The miscalibration can be time-varying due to the uncertainties in the elevation-nod gain calibration (BK–II) between each hour of observation. There are also gain variations that stay constant in time but vary among detector pairs. When making the full season map, the observed T map is correlated with the Planck T map to derive one overall normalization factor to calibrate the amplitude of the map, referred to as the absolute calibration (BK–II).

Variations of the actual absolute calibration values between detectors can translate into spatial amplitude modulation of the coadded maps. This amplitude variation could also be introduced by bandpass mismatches (BK–II) between pairs of detectors. Since the detector gain is calibrated with the atmospheric response, and the atmospheric emission and CMB have different spectra, a mismatch in detector bandpasses will lead to a gain mismatch in the observed CMB signal. The gain mismatches discussed above can also happen between intrapair detectors. In this case, instead of an amplitude modulation distortion $\tau(\hat{n})$, we will get monopole T to P leakage (or differential gain leakage), which corresponds to the $\gamma_1(\hat{n})$ and $\gamma_2(\hat{n})$ fields.

Miscalibration of the orientation of the detectors will translate to the rotation of the plane of polarization field $\alpha(\hat{n})$. The overall rotation of the map is calibrated out by minimizing the EB and TB spectra (BK–I). However, variations of the orientation from detector to detector can translate to an anisotropic rotation distortion field whose amplitude can be limited by the quadratic reconstructions.

The $f_1(\hat{n})$ and $f_2(\hat{n})$ fields can be generated from a coupling between a gain miscalibration and the boresight angle rotation (for a telescope with such capability). For example, if, at the

Table 4
A Summary of the Instrumental Systematics that Correspond to Each
Distortion Field in Equation (1)

Fields	Instrumental Systematics
τ	Detector gain miscalibration $(g_A + g_B)/2$
α	Detector polarization orientation miscalibration
f_1, f_2	Detector gain miscalibration coupled with boresight angle
$\boldsymbol{p}$	Beam center miscalibration
γ_1, γ_2	A/B detector differential gain $(g_A - g_B)/2$
d_1, d_2	A/B detector differential pointing $(\boldsymbol{b}_A - \boldsymbol{b}_B)/2$
q	A/B detector differential beam ellipticity

boresight angles that contribute more to the Q map, the detectors consistently exhibit a higher gain than the boresight angles that contribute more to the U map, we will effectively get a higher-amplitude Q map compared to U, which corresponds to an $f_1(\hat{\boldsymbol{n}})$ distortion. With the observation strategy of BK, different pairs of detectors cover different R. A. and decl. ranges on the sky. Therefore, gain variations among detector pairs can stochastically lead to $f_{1/2}(\hat{\boldsymbol{n}})$ distortion fields. Although there is no physical mechanism known to us that can produce this type of systematic coupling between the detector gains and the boresight angles in the BK experiments, we constrain f_1/f_2 for completeness.

The $\boldsymbol{p}(\hat{\boldsymbol{n}})$ ($\kappa(\hat{\boldsymbol{n}})/\omega(\hat{\boldsymbol{n}})$) fields capture changes in the CMB photon directions. The corresponding instrumental systematic is miscalibration of the beam center locations. In the main line analysis, the beam centers are derived from cross-correlating the observed T maps with the Planck T map (Section 11.9 of BK–II). Any miscalibration or uncertainty that varies from detector pair to detector pair will produce the $\boldsymbol{p}(\hat{\boldsymbol{n}})$ distortion fields.

The second line in Equation (1) involves T to P leakage. These distortions arise from a mismatch of the beams of pairs of orthogonal detectors A and B. Consider a Gaussian beam,

$$\mathcal{B}(\hat{\boldsymbol{n}}, \boldsymbol{b}, e) = \frac{1}{2\pi\sigma^2(1 - e^2)}$$
$$\times \exp\left[-\frac{1}{2\sigma^2}\left(\frac{(n_1 - b_1)^2}{(1 + e)^2} + \frac{(n_2 - b_2)^2}{(1 - e)^2} \right) \right],$$
$$(52)$$

where $\boldsymbol{b}$ is the beam offset, σ is the mean beamwidth, and e is the ellipticity in the direction of detector polarization (plus ellipticity). In the BK beam map measurements, the differential cross-ellipticities are subdominant compared to the differential plus ellipticities (Keck Array & BICEP2 Collaborations XI 2019). Therefore, the cross-ellipticity and its corresponding distortion field are ignored in this paper. A mismatch of the beam parameters between A and B will translate to the distortion fields as follows:

$$\sigma\boldsymbol{p} = (\boldsymbol{b}_A + \boldsymbol{b}_B)/2, \qquad (53)$$
$$\sigma\boldsymbol{d} = (\boldsymbol{b}_A - \boldsymbol{b}_B)/2, \qquad (54)$$
$$q = (e_A - e_B)/2. \qquad (55)$$

In Table 4, we summarize the correspondence of instrumental systematics to the distortion fields. To demonstrate the connection between the systematic effects and the distortion fields, we generate simulations that contain some of the systematic effects and reconstruct their distortion field spectra.
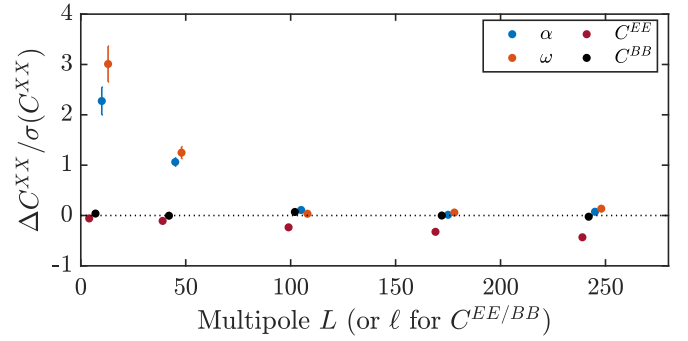

Figure 10. Mean shift in α, ω, EE, and BB spectra in simulations with a $10°$ random detector polarization angle scatter divided by the standard deviation of the nonrotated simulations. Here α and ω pick up a strong signal at low L, while C_ℓ^{EE} is suppressed at higher ℓ because the random per-detector polarization rotations average out near the center of the map and reduce the overall amplitude.

The systematic effects are added to the pair maps (BK–I) before the map coaddition step to reduce the cost of computation. The complete analysis is presented in Appendix B. Here we present two representative cases, one where the systematics are constant in time but vary over detectors (a $10°$ random Gaussian detector polarization angle rotation) and another where the systematics vary over time (10% random Gaussian differential gain fluctuation varying from hour to hour).

The shifts in the α, ω, EE, and BB spectra caused by the randomized detector rotation angles are shown in Figure 10. For the extreme $10°$ case, the simulated $C_L^{\alpha\alpha}$ shows a very strong signal at low L, while the BB spectrum remains unaffected. We stress that this is not true anymore if we did not calibrate the overall rotation of the maps, and there would be a nonzero mean angle calibration error causing a scale-dependent signal in the distortion field power spectrum (Mirmelstein et al. 2021). The curl component of the lensing field ω also detects the rotation field due to the correlation between the α and ω estimators.

In Figure 11, we show the spectra for γ_1, γ_2, EE, and BB for the 10% random differential gain fluctuations. Compared to the detector angle rotation where the instrumental effect is constant in time but varies over detector pairs, the time-varying gain mismatch simulations generate distortion powers that are distributed over a wider range of multipoles. This systematic T to P leakage shows up strongly in both γ and BB.

In Appendix B, we observe that other kinds of systematics that are constant in time but vary over detectors also generate distortions at large scales (low L). This is because each detector pair covers a significant portion of the map, and variations among detector pairs therefore primarily create large-scale distortions. On the other hand, time-varying instrumental systematics can generate distortion power over a much wider range of multipoles. Depending on the type of systematic effects being studied, we can design systematics tests that focus on different multipole ranges of the distortion field spectra.

6.2. Quadratic Estimators versus BB Power Spectra for Detecting Distortion Fields

In the main line analysis (BK–I; BK–V; BK–VI), EE, BB, and EB spectra of map difference splits are used to test for instrumental systematics. In this section, comparisons are made between BB power spectra and quadratic estimators in their
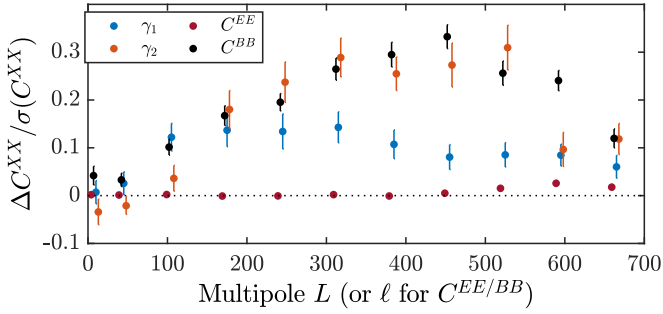
Figure 11. Mean shift in γ_1, γ_2, *EE*, and *BB* spectra in simulations with a 10% Gaussian fluctuation of differential gain that varies from detector pair to detector pair and hour to hour divided by the standard deviation of the nonfluctuated simulations.

ability to detect various systematics. We highlight cases in which the latter are more sensitive at detecting the spurious *B*-mode produced by the distortion fields. To that end, we generate simulations with Gaussian realizations of distortion fields within a narrow range of multipoles ($\Delta L = 50$). Any Gaussian distortion field with a smooth spectrum can be considered as a combination of multiple ΔL distortions,

$$C_L^{DD} = \begin{cases} A_D^2 & (L_{\min} \leqslant L \leqslant L_{\max}) \\ 0 & (\text{otherwise}) \end{cases}. \tag{56}$$

To make sensitivity comparisons between quadratic *EB/TB* estimators versus *BB* power spectra, we use distortion field simulations with different *L* range inputs as the fiducial model and see how well the amplitude of those fiducial distortion spectra can be constrained by the standard simulations (undistorted lensed-ΛCDM+dust+noise). We define the sensitivity ratio as

$$\hat{A}_D^{XX'} = \frac{\sum_{bb'} \hat{C}_b^{XX'} \text{Cov}_{bb'}^{-1} C_{b'}^{XX',f}}{\sum_{bb'} C_b^{XX',f} \text{Cov}_{bb'}^{-1} C_{b'}^{XX',f}}, \tag{57}$$

$$\text{sensitivity ratio} = \frac{\sigma(A_D^{BB})}{\sigma(A_D^{EB/TB})}, \tag{58}$$

where XX' represents *EB*, *TB*, or *BB*; $C_b^{EB/TB}$ are the distortion field reconstruction bandpowers (four-point) from quadratic *EB/TB* estimators; C_b^{BB} are the two-point *BB* bandpowers; C_b^f stands for the mean bandpower from the distortion simulations characterized by Equation (56), which we take as the "signal" of the particular systematic effect that we want to measure or constrain; and $\sigma(A_D)$ is the standard deviation of the best-fit A_D amplitude for the level of systematics from the 499 undistorted lensed-ΛCDM+dust+noise simulations. The estimator that is more sensitive in detecting the systematics will have a larger signal-to-noise ratio in measuring the amplitude $\hat{A}_D$ and therefore a smaller $\sigma(A_D)$ value. When the sensitivity ratio defined in Equation (58) is greater than 1, the quadratic estimator is more sensitive than the *BB* power spectrum at detecting the particular distortion at that angular scale.

In Figure 12, we demonstrate that the quadratic estimators are more sensitive than the *BB* power spectrum at detecting the distortion fields between $L = 1$ and 400. For all distortion fields, the quadratic estimators perform better when the distortion power is at a larger scale (lower *L*). Among the
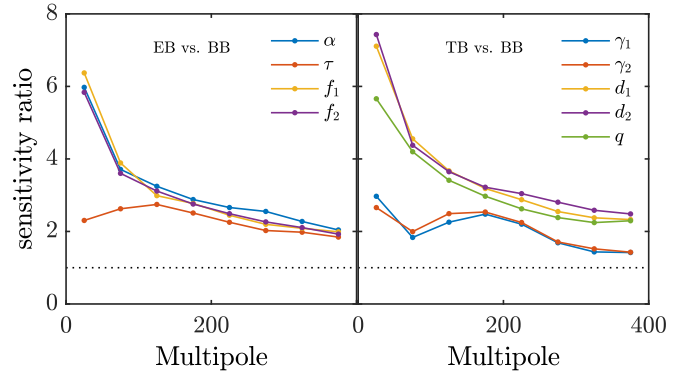

Figure 12. Sensitivity ratio as defined in Equation (58). A sensitivity ratio $\sigma(A_D^{EB})/\sigma(A_D^{BB})$ above 1 means that the quadratic estimator is more sensitive than the *BB* spectrum at detecting the distortion field at that angular scale. The left panel shows the sensitivity ratio for the fields involving only the polarization, while the right panel shows the fields involving *T*.

polarization-only distortions, α, f_1, and f_2 in particular are detected by the *EB* quadratic estimators with high sensitivity relative to the *BB* spectra. The distortions involving CMB temperature, d_1, d_2, and q are also very sensitively measured by the *TB* quadratic estimators. The above is as we would like it to be; we can detect systematics using the distortion fields before they significantly bias the *BB* spectrum.

Since we are reconstructing all of the distortion field spectra C_L^{DD} simultaneously, and the different distortion fields are not necessarily orthogonal to each other, it is important to study whether any spurious signal detected by a particular D_1 estimator can be reliably pointed to as an actual distortion signal from that field. To this end, we use the same set of simulations described by Equation (56) to test for the cross-sensitivity or correlation between the different distortion fields. We define the sensitivity ratio the same way as in Equation (58), but in this analysis, a different quadratic estimator D_2 is applied to try to detect the D_1 distortion input.

In Figure 13, we show the correlation between different distortion fields using the $L = 1$–50 distortion simulations with the diagonal normalized to 1. The fact that the diagonal terms are much larger than the off-diagonal terms means that the distortions would be much more strongly detected with the corresponding quadratic estimator before they are detected by another estimator. One exception is the correlation of q with d_1/d_2 at low *L*. The existence of a large *T* to *P* dipole leakage can swamp the q estimator, as we will see in Section 6.5.

6.3. Effects of Point-source Contamination

The brightest point sources at the frequencies relevant for CMB observations are flat-spectrum radio sources (Battye et al. 2011). Since these point sources are brighter at lower frequencies relative to the CMB spectrum, the 95 GHz data set is much more affected by point sources in the distortion field analysis.

We estimate the effect of point-source contamination in the distortion field analysis by injecting simulated point sources from a preliminary catalog obtained by private communication with the SPT-3G collaboration. The fluxes are taken from preliminary SPT-3G 95 GHz data and are, on average, 2.5% polarized with an approximately exponential distribution. The *T*, *Q*, and *U* fluxes are converted to equivalent CMB temperatures and added to the pixels closest to the location
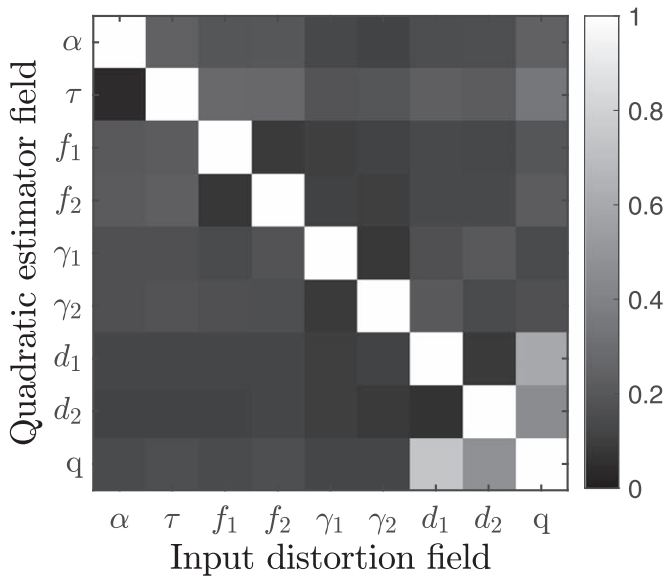
Figure 13. Correlation matrix of the sensitivity ratio as defined in Equation (58) for all combinations of input distortion and quadratic estimators. The results plotted use distortion input from $L = 1$ to 50. The horizontal axis shows the input distortion field injected in the simulations, and the vertical axis shows the quadratic estimators used to detect the signal. We see that q and d_1/d_2 have the strongest correlations, but in general, all of the distortion signals are best measured with their own estimators.

of the sources in the input map. The BICEP3 beam and observation matrix R are then applied to generate a point-source simulation map (Equation (14)). We find that the mean shift of the *EB* distortion spectra caused by these point sources is negligible. However, the 95 GHz *TB* estimators strongly detect the point sources, with the brightest few accounting for most of the contribution.

From this simulation, we determine that the point-source contribution becomes negligible after masking the 20 sources with the highest polarized fluxes. These are then added to the apodization mask by injecting Gaussian divots with $0°.5$ width at the 20 locations. In Table 5, the χ/χ^2 PTEs for the real data, with and without the point-source mask, for the *TB* estimators are listed. We find that the point-source mask is necessary for the BICEP3 95 GHz data to pass the distortion field systematics tests but does not affect the BICEP2/Keck 150 GHz data much.

In BK–XIII, Appendix F, it is estimated that the polarized flux from point sources may produce a bias on r at a level of ≈ 1–3×10^{-3}. While small compared to our present uncertainties, point-source contamination and its mitigation will become more important in future analysis, and the *TB* quadratic estimators can be a powerful diagnostic tool. In Appendix E, we discuss the reasons why *TB* quadratic estimators are sensitive to polarized point sources, derive estimators that are even more powerful for detecting point sources, and compare the performance of the different estimators at point-source detection.

6.4. Distortion Field Systematics Tests on BK Real Data

With the connections between the various systematics and distortion fields established, in this section, we present the results of the distortion field systematics tests for the two real data maps at 95 and 150 GHz. The distortion field systematics tests are performed with the same method as in Section 5.4.3 and Equations (47) and (48). The only difference is that the

Table 5
The χ/χ^2 PTEs with and without Point-source Masks (PSM) for the *TB*-reconstructed Distortion Fields

Field	95 GHz (χ/χ^2 PTE)		150 GHz (χ/χ^2 PTE)	
	w/o PSM	with PSM	w/o PSM	with PSM
d_1	0.02/0.01	0.45/0.08	0.69/0.88	0.56/0.88
d_2	0.03/0.40	0.54/0.63	0.84/0.99	0.97/0.83
γ_1	**7.3e-04/0.13**	0.09/0.41	0.07/0.12	0.18/0.06
γ_2	0.52/1.00	0.78/0.98	0.03/0.06	0.05/0.08
q	0.22/0.04	0.48/0.63	0.22/0.53	0.63/0.80

Note. The bold value is derived from the theoretical χ distribution, since the observed value is outside of the 499 simulation distribution. The point-source mask removes the brightest 20 sources in polarization according to a preliminary SPT-3G catalog. Without the point-source mask, 95 GHz would fail the γ_1 systematics test and in general have lower PTEs. For 150 GHz, there is no significant change to the PTEs.

bandpowers $\hat{C}_b$ here correspond to the reconstructions from the full *E* and *B* map instead of the jackknife *B* map. In Figure 14, we plot the difference of the real data reconstructed distortion field bandpowers and the mean of the simulations divided by the standard deviation of the simulations to show the significance of detection.

The C_L^{DD} spectra use the realization-dependent bias estimation outlined in Section 4.3. For the fields reconstructed with *TB* estimators (right panel of Figure 14), we substitute in the same observed *T* map for all of the simulations. This is because the standard lensed-ΛCDM simulations are constrained to the real CMB *T* map (BK–I), and *T* is measured with such a high signal-to-noise ratio that the noise contribution is negligible. Since we are much more interested in testing for systematics in our *B* map than the *T* map, we elect to fix to the same extremely well-measured observed BK *T* map for both observation and simulations.

With the $\hat{C}_L^{DD}$ in Figure 14, we evaluate the χ and χ^2 PTEs. We list these values in Table 6 and show histograms in Figure 15. All of the χ and χ^2 values lie within the 499 simulation distributions. There is one low PTE at 0.002 for the χ^2 of f_2 from 95 GHz. Examining the spectra in Figure 14, the low χ^2 PTE can be traced to the second bandpower that fluctuates high. With the same method as in Equations (49)–(51), we take into account the look-elsewhere effect and evaluate the global PTE statistic that compares the most extreme value among the 44 numbers in Table 6 to the simulations. We find that the probability of getting a global value of less than 0.002 is 0.08, offering no evidence for contamination in the data.

6.5. Effectiveness of Deprojection

As discussed in Section 6.1, many of the distortion fields correspond to specific forms of beam mismatch. Beam systematics have been very important and well studied in the BK experiments (BK–III). Starting from BICEP2, the deprojection method has been developed to filter out potentially spurious signals that correspond to *T* to *P* leakage modes (BK–I; BK–VII). We have also carried out extensive far-field beam measurement campaigns every year, as well as published a beam systematics paper to model and quantify how the beam systematics can affect the measurement of the tensor-to-scalar ratio r (Keck Array & BICEP2 Collaborations XI 2019).
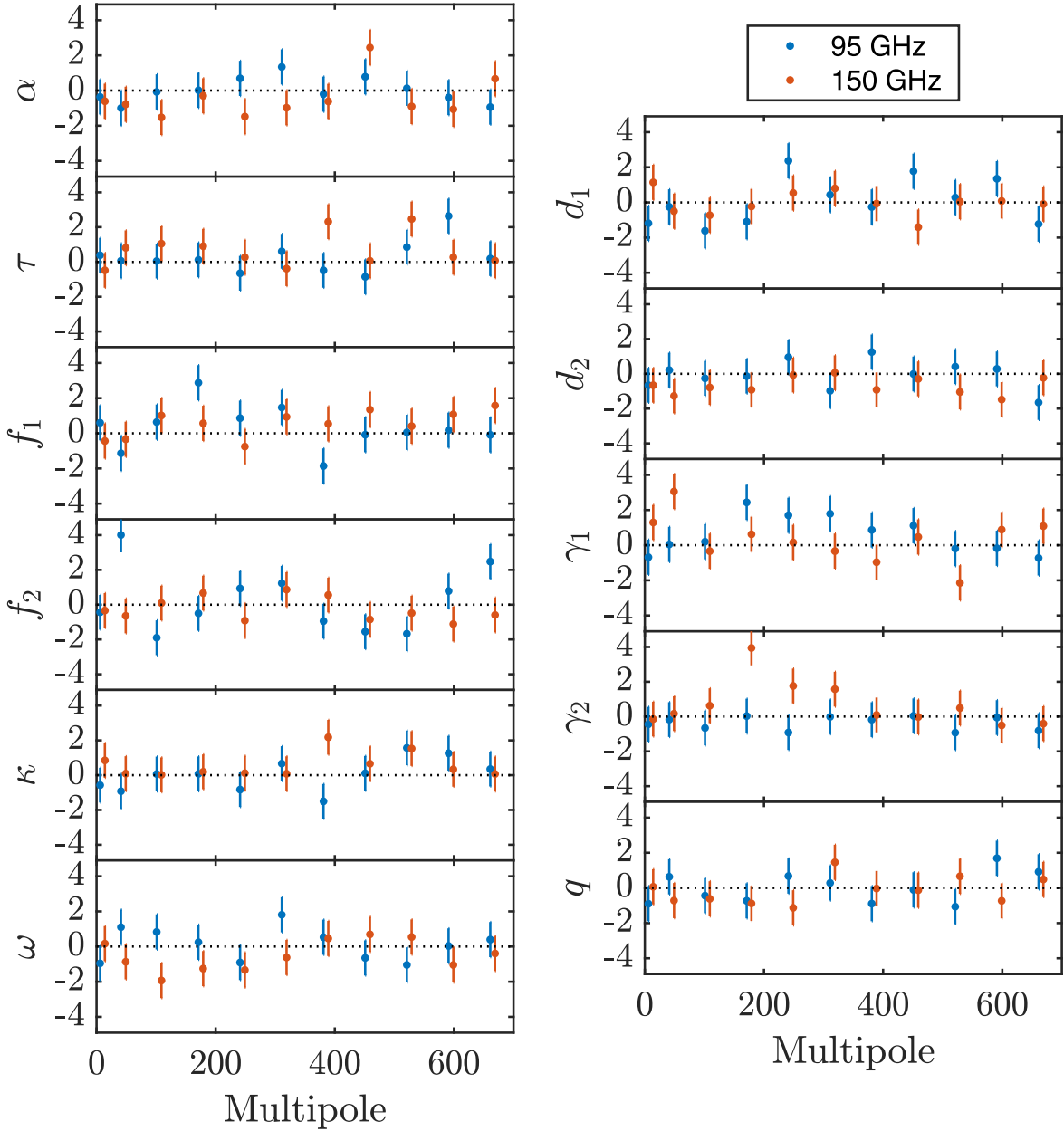
Figure 14. Fractional deviations of the 11 real data distortion field bandpowers $(\hat{C}_L^{DD} - \bar{C}_L^{DD})/\sigma(\hat{C}_L^{DD})$. The plots on the left are reconstructed with the *EB* quadratic estimators, while the ones on the right are reconstructed with the *TB* estimators and have the point-source mask applied. The corresponding χ and χ^2 PTEs are listed in Table 6.

In Section 6.4, with the standard differential gain and pointing deprojection, the distortion field *TB* systematics tests pass with no evidence of any residual *T* to *P* leakage. We will now investigate whether the distortion field quadratic estimators can detect any spurious signal if we do not perform the differential gain and pointing deprojections. With the data products available on disk, it is simple to add the components that are filtered out by the deprojections back in and construct maps without deprojection. We then perform the same χ/χ^2 distortion field systematics tests by comparing the observed $\hat{C}_L^{DD}$ with the simulations.

In Figure 16, the BICEP2/Keck 150 GHz maps spectacularly fail the d_1, d_2, and q systematics tests without differential pointing deprojection. On the other hand, the BICEP3 95 GHz maps have much lower differential pointing and do not see much of a change in the reconstructed spectra when differential pointing deprojection is turned off. Without differential gain, however, we would detect a strong large-scale γ_2 distortion in 95 GHz. We note that the differential pointing systematic in 150 GHz is also strongly detected by the q *TB* estimator. This is consistent with the results in Figure 13, where we showed that q has significant correlation with d_1 and d_2 at large scales.

In Table 7, we show the χ and χ^2 PTEs for different deprojection options. In general, the χ and χ^2 PTEs decrease when either differential gain or differential pointing deprojection is disabled. This offers strong evidence that the deprojections are indeed successful in filtering out the monopole and dipole *T* to *P* leakage in the real data when compared to simulations with no such systematics. We note that the suite of jackknife tests for the power spectrum analysis
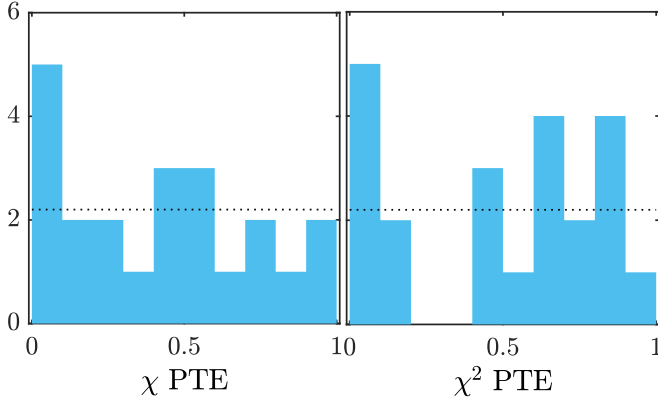
Figure 15. Distributions of the distortion systematics test χ and χ^2 PTEs in Table 6.

includes targeted tests to detect these types of systematic contamination, which would lead to the same conclusion.

7. Conclusions

The line-of-sight distortion effects of the CMB can be characterized to first order with 11 fields. Three of these correspond to known or conjectured cosmological signals: gravitational lensing and $\kappa(\hat{\boldsymbol{n}})$, patchy reionization and $\tau(\hat{\boldsymbol{n}})$, and cosmic birefringence and $\alpha(\hat{\boldsymbol{n}})$. Combining the sensitivity from our two deepest maps, 150 GHz from BICEP2/Keck and 95 GHz from BICEP3, we constrained physical models that can generate these distortion fields. For gravitational lensing, we measured the lensing amplitude to be $A_L^{\phi\phi} = 0.97 \pm 0.19$, which is a factor of 2 improvement from our previous results in BK–VIII. For cosmic birefringence, we constrained the amplitude of cosmic birefringence and the related cosmological parameters to $A_{CB} \leqslant 0.044$, $g_{a\gamma} \leqslant 2.6 \times 10^{-2}/H_I$, and $B_{1\mathrm{Mpc}} \leqslant 6.6$ nG. This is a factor of 3 improvement on $g_{a\gamma}$ and a factor of 4 improvement for $B_{1\mathrm{Mpc}}$ compared to our previous BK–IX (BK14) analysis, resulting in the tightest constraint to date from the CMB four-point function. For patchy reionization, while not competitive compared to the Planck TT results (Namikawa 2018), we achieved the best constraint with CMB polarization on the $\tau(\hat{\boldsymbol{n}})$ amplitude.

Treating the distortion fields as systematics tests, we demonstrated with simulations the connections between the distortion fields and the various instrumental effects in experiments with similar designs to BK. We further show that the *EB/TB* distortion field estimators are more sensitive than the *BB* spectrum at detecting random Gaussian realizations of distortions, especially at larger scales. Additionally, we find that the *TB* estimators are very sensitive to contamination from polarized point sources.

We perform instrumental systematics tests on the 95 and 150 GHz maps by comparing the distortion field bandpowers of the real data to lensed-ΛCDM+dust+noise simulations and confirm that the 11 observed distortion spectra are consistent with the simulations. We also verify that the differential gain and pointing deprojections in our standard mapmaking pipeline are effective at filtering out the T to P leakage. Without the differential gain deprojection, we would detect an excess γ_2 power in the 95 GHz map, while without differential pointing deprojection, we would detect a very strong excess in the q, d_1, and d_2 fields of the 150 GHz map. This also confirms that the quadratic estimators are powerful tools to guard against T to P

Table 6
χ and χ^2 PTEs Derived from the Distortion Field Spectra Shown in Figure 14

Field	95 GHz PTE		150 GHz PTE	
	χ	χ^2	χ	χ^2
α	0.50	0.90	0.90	0.18
τ	0.22	0.43	0.04	0.19
f_1	0.20	0.09	0.08	0.65
f_2	0.26	0.002	0.75	0.84
κ	0.48	0.53	0.08	0.73
ω	0.36	0.48	0.92	0.62
d_1	0.45	0.08	0.56	0.88
d_2	0.54	0.63	0.97	0.83
γ_1	0.09	0.41	0.18	0.06
γ_2	0.78	0.98	0.05	0.08
q	0.48	0.63	0.63	0.80

Note. The results of *TB* estimators are derived with the point-source mask applied; therefore, the PTEs from d_1 to q are identical to the "with PSM" case of Table 5. The global PTE for the most extreme χ/χ^2 PTE (0.002 here) is 0.08.

Table 7
χ and χ^2 PTEs Derived from the Distortion Field Spectra Shown in Figure 16

	95 GHz PTE (χ/χ^2)		
Field	Standard	No Diff. Gain	No Diff. Point.
d_1	0.45/0.08	0.69/0.06	0.24/0.14
d_2	0.54/0.63	0.56/0.63	0.45/0.24
γ_1	0.09/0.41	0.08/0.49	0.13/0.43
γ_2	0.78/0.98	0.22/**2e-13**	0.76/0.99
q	0.48/0.63	0.51/0.46	0.34/0.36
	150 GHz PTE (χ/χ^2)		
Field	Standard	No Diff. Gain	No Diff. Point.
d_1	0.56/0.88	0.11/0.42	**7e-05**/**1e-49**
d_2	0.97/0.83	0.38/0.88	**2e-39**/**<1e-99**
γ_1	0.18/0.06	0.002/0.008	0.03/0.04
γ_2	0.05/0.08	0.01/0.07	0.006/0.002
q	0.63/0.80	0.06/0.27	**7e-70**/**<1e-99**

Note. The bold numbers are derived from theoretical χ and χ^2 distributions when the real values are outside of the 499 simulation distributions.

leakage systematics in the absence of differential gain and pointing deprojections.

With this first demonstration of quadratic estimators as instrumental systematics diagnostics on real data, we pave the way toward their future application as tools to self-calibrate upcoming data sets (Yadav et al. 2010; Williams et al. 2021).
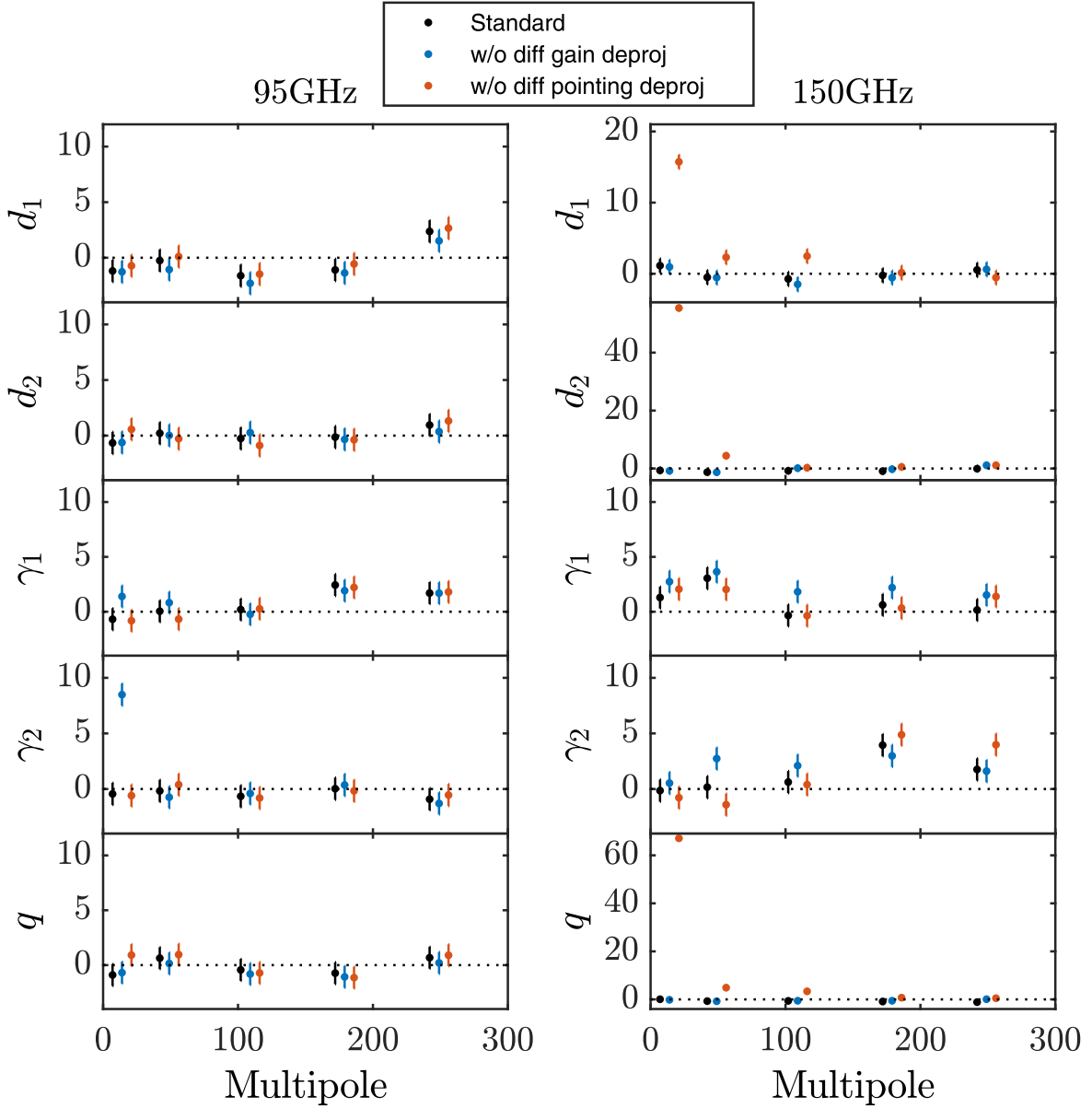
Figure 16. Fractional deviations of the 11 real data distortion field bandpowers $(\hat{C}_L^{DD} - \bar{C}_L^{DD})/\sigma(\hat{C}_L^{DD})$ with and without the differential gain and pointing deprojections. Here 95 GHz fails the γ_2 systematics test without differential gain deprojection, and 150 GHz fails the d_1, d_2, and q systematics tests without differential pointing deprojection.

Appendix A
Minimal Quadratic Estimators of Distortion Fields

We follow Yadav et al. (2010) and construct a minimum variance quadratic estimator of the distortion field from *EB* and *TB* correlations. See Equation (1) for the definitions of the distortions. A scalar field such as CMB temperature *T* can be expanded in the Fourier basis as

$$T_l = \int d\hat{n}\, T(\hat{n}) e^{-i\boldsymbol{l}\cdot\hat{n}}. \tag{A1}$$

A complex field $(S_1 \pm iS_2)(\hat{n})$ of spin $\pm s$ can be expanded in the Fourier harmonics basis as

$$[S_a \pm iS_b]_l = (\pm 1)^s \int d\hat{n}\, [S_1(\hat{n}) \pm iS_2(\hat{n})] e^{\mp si\phi_l} e^{-i\boldsymbol{l}\cdot\hat{n}}, \tag{A2}$$

Table 8
Weights and Filters for the Different Distortion Fields, Where $\phi_l = \cos^{-1}(\hat{\boldsymbol{n}} \cdot \hat{\boldsymbol{l}})$ (Yadav et al. 2010)

D	$f^{EB}_{l_1,l_2}$	$f^{TB}_{l_1,l_2}$	$W^B_{l_1,l_2}$	$W^E_{l_1,l_2}$
τ	$\tilde{C}^{EE}_{l_1}\sin 2(\phi_{l_1}-\phi_{l_2})$	$\tilde{C}^{TE}_{l_1}\sin 2(\phi_{l_1}-\phi_{l_2})$	$\sin 2(\phi_{l_2}-\phi_L)$	$\cos 2(\phi_{l_2}-\phi_L)$
α	$2\tilde{C}^{EE}_{l_1}\cos 2(\phi_{l_1}-\phi_{l_2})$	$2\tilde{C}^{TE}_{l_1}\cos 2(\phi_{l_1}-\phi_{l_2})$	$2\cos 2(\phi_{l_2}-\phi_L)$	$-2\sin 2(\phi_{l_2}-\phi_L)$
γ_a	$\tilde{C}^{TE}_{l_1}\sin 2(\phi_L-\phi_{l_2})$	$\tilde{C}^{TT}_{l_1}\sin 2(\phi_L-\phi_{l_2})$	$\sin 2(\phi_{l_1}-\phi_L)$	$\cos 2(\phi_{l_1}-\phi_L)$
γ_b	$\tilde{C}^{TE}_{l_1}\cos 2(\phi_L-\phi_{l_2})$	$\tilde{C}^{TT}_{l_1}\cos 2(\phi_L-\phi_{l_2})$	$\cos 2(\phi_{l_1}-\phi_L)$	$-\sin 2(\phi_{l_1}-\phi_L)$
f_a	$\tilde{C}^{EE}_{l_1}\sin 2(2\phi_L-\phi_{l_1}-\phi_{l_2})$	$\tilde{C}^{TE}_{l_1}\sin 2(2\phi_L-\phi_{l_1}-\phi_{l_2})$	$\sin 2(2\phi_{l_1}-\phi_{l_2}-\phi_L)$	$\cos 2(2\phi_{l_1}-\phi_{l_2}-\phi_L)$
f_b	$\tilde{C}^{EE}_{l_1}\cos 2(2\phi_L-\phi_{l_1}-\phi_{l_2})$	$\tilde{C}^{TE}_{l_1}\cos 2(2\phi_L-\phi_{l_1}-\phi_{l_2})$	$\cos 2(2\phi_{l_1}-\phi_{l_1}-\phi_L)$	$-\sin 2(2\phi_{l_1}-\phi_{l_1}-\phi_L)$
Ω	$-\tilde{C}^{EE}_{l_1}\sigma(\boldsymbol{l}_1\times\hat{\boldsymbol{L}})\sin 2(\phi_{l_1}-\phi_{l_2})$	$-\tilde{C}^{TE}_{l_1}\sigma(\boldsymbol{l}_1\times\hat{\boldsymbol{L}})\sin 2(\phi_{l_1}-\phi_{l_2})$	$\sigma(\boldsymbol{l}_2\times\hat{\boldsymbol{l}}_1)\cdot\hat{\boldsymbol{z}}\sin 2(\phi_{l_2}-\phi_L)$	$\sigma(\boldsymbol{l}_2\cdot\hat{\boldsymbol{l}}_1)\sin 2(\phi_{l_2}-\phi_L)$
Φ	$-\tilde{C}^{EE}_{l_1}\sigma(\boldsymbol{l}_1\cdot\hat{\boldsymbol{L}})\sin 2(\phi_{l_1}-\phi_{l_2})$	$-\tilde{C}^{TE}_{l_1}\sigma(\boldsymbol{l}_1\cdot\hat{\boldsymbol{L}})\sin 2(\phi_{l_1}-\phi_{l_2})$	$\sigma(\boldsymbol{l}_2\cdot\hat{\boldsymbol{l}}_1)\sin 2(\phi_{l_2}-\phi_L)$	$\sigma(\boldsymbol{l}_2\times\hat{\boldsymbol{l}}_1)\cdot\hat{\boldsymbol{z}}\sin 2(\phi_{l_2}-\phi_L)$
d_a	$\tilde{C}^{TE}_{l_1}(l_1\sigma)\cos 2(\phi_L+\phi_{l_1}-2\phi_{l_2})$	$\tilde{C}^{TT}_{l_1}(l_1\sigma)\cos 2(\phi_L+\phi_{l_1}-2\phi_{l_2})$	$-(l_2\sigma)\cos(\phi_{l_1}+\phi_{l_2}-2\phi_L)$	$-(l_2\sigma)\sin(\phi_{l_1}+\phi_{l_2}-2\phi_L)$
d_b	$-\tilde{C}^{TE}_{l_1}(l_1\sigma)\sin 2(\phi_L+\phi_{l_1}-2\phi_{l_2})$	$-\tilde{C}^{TT}_{l_1}(l_1\sigma)\sin 2(\phi_L+\phi_{l_1}-2\phi_{l_2})$	$(l_2\sigma)\sin(\phi_{l_1}+\phi_{l_2}-2\phi_L)$	$(l_2\sigma)\cos(\phi_{l_1}+\phi_{l_2}-2\phi_L)$
q	$-\tilde{C}^{TE}_{l_1}(l_1\sigma)^2\sin 2(\phi_{l_1}-\phi_{l_2})$	$-\tilde{C}^{TT}_{l_1}(l_1\sigma)^2\sin 2(\phi_{l_1}-\phi_{l_2})$	$-(l_2\sigma)^2\sin 2(\phi_{l_2}-\phi_L)$	$-(l_2\sigma)^2\cos 2(\phi_{l_2}-\phi_L)$

Note. Here $f^{D,XB}_{l_1,l_2}$ are the filter functions in Equation (19), and the weight functions $W^B_{l_1,l_2}$ describe the B-modes generated from the distortions in Equations (A4) and (A6). See Equations (15) and (A3) for the relation between the Fourier harmonic basis with subscript a/b and the Fourier transform of the distortion fields with subscript $1/2$.

where $\phi_l = \cos^{-1}(\hat{\boldsymbol{n}} \cdot \hat{\boldsymbol{l}})$. We can also directly Fourier transform the $S_1 \pm iS_2(\hat{\boldsymbol{n}})$ fields as

$$[S_1 \pm iS_2]_l = \int d\hat{\boldsymbol{n}}[S_1(\hat{\boldsymbol{n}}) \pm iS_2(\hat{\boldsymbol{n}})]e^{-il\cdot\hat{\boldsymbol{n}}}. \tag{A3}$$

One well-known example is the transformation from Q, U in map space to the Q_l, U_l, E_l, B_l Fourier modes. In this case, $(S_1 \pm iS_2)(\hat{\boldsymbol{n}}) = (Q \pm iU)(\hat{\boldsymbol{n}})$ is a spin ± 2 field. Its Fourier transform is $(Q_l \pm iU_l)$, and its Fourier harmonics are $(E_l \pm iB_l)$. The Fourier harmonics are not dependent on the coordinates, whereas the direct Fourier transforms of the individual spin fields will transform into each other with a rotation of the coordinates.

For f_1/f_2, d_1/d_2, and γ_1/γ_2, we reconstruct Fourier transform quantities that are coordinate-dependent. They are used as systematics checks, and it is convenient to be able to connect them directly to the Q and U maps. For the lensing deflection $\boldsymbol{p}$, we reconstruct the curl (Ω) and gradient (Φ) components, which are independent of the coordinates. Assuming a zero primordial B-mode, we write down to leading order the E_L and B_L with a distortion field D,

$$B_L = \int \frac{d^2l_1}{(2\pi)^2} D_{l_1}\tilde{E}_{l_2}W^B_{l_1,l_2}, \tag{A4}$$

$$E_L = \tilde{E}_L + \int \frac{d^2l_1}{(2\pi)^2} D_{l_1}\tilde{E}_{l_2}W^E_{l_1,l_2}, \tag{A5}$$

where $\boldsymbol{l}_2 = \boldsymbol{L} - \boldsymbol{l}_1$, and W^B, W^E are weights that can be derived for the individual distortion fields. Similarly, the E_L and B_L generated by the distortions that can be sourced by T to P leakage ($\gamma_{1/2}$, $d_{1/2}$, q) are written as

$$B_L = \int \frac{d^2l_1}{(2\pi)^2} D_{l_1}\tilde{T}_{l_2}W^B_{l_1,l_2}, \tag{A6}$$

$$E_L = \tilde{E}_L + \int \frac{d^2l_1}{(2\pi)^2} D_{l_1}\tilde{T}_{l_2}W^E_{l_1,l_2}, \tag{A7}$$

where the weights $W^B_{l_1,l_2}$ for generating B-modes are listed in Table 8.

For the primordial undistorted CMB fields, the power spectra are

$$\langle X_{l_1}X'_{l_2} \rangle = (2\pi)^2\delta(\boldsymbol{l}_1 + \boldsymbol{l}_2)\tilde{C}^{XX'}_{l_1}, \tag{A8}$$

where $X, X' = T, E, B$, and $\langle \tilde{E}_{l_1}\tilde{B}_{l_2} \rangle = 0$, $\langle \tilde{T}_{l_1}\tilde{B}_{l_2} \rangle = 0$. From Equations (A4) and (A6), we can calculate the ensemble $\langle X_{l_1}B_{l_2} \rangle$ correlation averaged over CMB realizations,

$$\langle X_{l_1}B_{l_2} \rangle_{\text{CMB}} = f^{D,XB}_{l_1,l_2}D_L, \tag{A9}$$

where the filter functions $f^{D,XB}$ are listed in Table 2 for $X = T/E$, and $\boldsymbol{L} = \boldsymbol{l}_1 + \boldsymbol{l}_2$.

There is only one universe and one CMB realization available for observation. However, given an L, there are many different combinations of $\boldsymbol{l}_1$ and $\boldsymbol{l}_2$ that satisfy $\boldsymbol{l}_1 + \boldsymbol{l}_2 = \boldsymbol{L}$. Therefore, we can write down a linear combination of $X_{l_1}B_{l_2}$ with some weight factor $F^{D,XB}_{l_1,l_2}$ that would minimize the variance of the $\hat{D}_L \propto \int d^2l_1 X_{l_1}B_{l_2}F^{D,XB}_{l_1,l_2}$ estimator. The weight $F^{D,XB}_{l_1,l_2}$ can be derived from

$$\frac{\partial}{\partial F^{D,XB}_{l_1,l_2}}\langle |\hat{D}^{XB} - D|^2 \rangle_{\text{CMB, distortions}} = 0, \tag{A10}$$

where the brackets stand for the average over both CMB and distortion field realizations.

For $X = E$ or T, $\tilde{C}^{XB}_l = 0$. In this case,

$$F^{D,XB}_{l_1,l_2} = \frac{f^{D,XB}_{l_1,l_2}}{C^{XX}_{l_1}C^{BB}_{l_2}}, \tag{A11}$$

where $f^{D,XB}$ is exactly the factor in Equation (A9), and $C^{XX}_{l_1}$, $C^{BB}_{l_2}$ are the total observed power including contributions from the noise and distortion fields (usually just lensing). Up to a normalization factor $A^{D,XB}_L$, the quadratic estimator for the distortion field can be written as

$$\bar{D}^{XB}_L = A^{D,XB}_L \int \frac{d^2l_1}{(2\pi)^2} X_{l_1}B_{l_2}F^{D,XB}_{l_1,l_2}, \tag{A12}$$

where $L = l_1 + l_2$, and the analytical form for the normalization factor $A_L^{D,XB}$ is

$$A_L^{D,XB} = \left[\int \frac{d^2 l_1}{(2\pi)^2} f_{l_1,l_2}^{D,XB} F_{l_1,l_2}^{D,XB} \right]^{-1}$$

$$= \left[\int \frac{d^2 l_1}{(2\pi)^2} \frac{(f_{l_1,l_2}^{D,XB})^2}{C_{l_1}^{XX} C_{l_2}^{BB}} \right]^{-1}. \qquad (A13)$$

The mean-field bias $\langle \bar{D}_L^{XB} \rangle$ is estimated from the simulations. After applying the correction for the mean-field bias, we have

$$\hat{D}_L^{XB} = \bar{D}_L^{XB} - \langle \bar{D}_L^{XB} \rangle. \qquad (A14)$$

Appendix B
Simulations of Systematic Effects that Generate Line-of-sight Distortions

In Section 6.1, we presented results for systematics simulations of random polarization and differential gain fluctuations. In this Appendix, we show the results from two more systematics simulations and offer a more in-depth discussion of each of the systematic effects. The four systematics simulations are as follows.

1. A 10° random detector polarization angle rotation (Figure 17(a)).
2. A 20% random pair-averaged detector gain fluctuations (Figure 17(b)).
3. A 10% random differential gain fluctuation varying from hour to hour (Figure 17(c)).
4. Dipole component of the T to P leakage from beam map simulations (Figure 17(d)).

The well-designed BK observation strategy leads to a very high degree of cancellation of systematics with an increasing number of detectors and observing time. Since the purpose of these simulations is to clearly establish the connections between the different instrument systematics and the distortion fields, we inject large systematic errors in the polarization rotation, gain fluctuation, and differential gain. The simulations are for BICEP3 95 GHz except for the beam map simulations, where we have simulations for both 95 and 150 GHz. In each figure, the error bars represent the scatter on the mean spectra over 49 realizations of the systematics simulations. For clarity, we only show the distortion field spectra that are expected to detect the injected systematics. The distortion spectra that are not plotted do not show an elevated signal.

For the detector polarization angle errors, we generate misestimated angles by drawing from a Gaussian distribution of mean zero and standard deviation of 10° for each detector pair for the entire observing season. We rotate the detector polarization angle assumed in the mapmaking by these angles to produce a set of simulations including polarization angle systematics. The shift in the α, ω, EE, and BB spectra caused by the random detector rotation is shown in Figure 17(a). Unsurprisingly, the random detector angle rotation creates a washout effect that reduces C_ℓ^{EE}. However, the reduction caused by the washout effect and the distortion-generated BB power roughly cancel, leaving the total C_ℓ^{BB} largely unchanged. For the distortion reconstruction spectra of the random rotation simulations, $C_L^{\alpha\alpha}$ shows a strong signal at low L, as expected.

However, ω also detects the rotation field due to the strong correlation between the α and ω estimators.

For the pair-averaged gain systematics, we simulate a 20% random Gaussian fluctuation on the pair gain. The injected relative gain error is constant over time and only varies from detector pair to detector pair. Due to the observation strategy, most of the detector pairs do not cover the same sky area at multiple boresight rotation angles. This means that a gain fluctuation over detector pairs also sporadically generates f_1 and f_2 distortions in addition to the amplitude modulation τ field. We show the f_1, f_2, τ, EE, and BB spectra generated by the gain fluctuation in Figure 17(b). We observe a clear signal in f_1 and f_2 that corresponds to the injected systematics. However, we do not detect excess power in τ, as one naively expects. One reason is that the τ EB estimator is not sensitive enough to detect the distortion effect at the level of 20% gain fluctuation with only 49 realizations of the systematics simulation. Another reason is the smooth apodization mask combined with the purification matrix that degrades the sensitivity to τ at the lowest multipole range, where most of the τ distortion power is expected.

For the gain mismatches (differential gain) between detector pairs, we simulate a 10% random Gaussian fluctuation in $(g_A - g_B)/2$ for every detector pair and hour of observation. One possible contribution to gain mismatch is the uncertainties in the elevation nod–derived calibration factors (BK–I). With the differential gain deprojection that removes T to P leakage over 10 hr timescales, residual systematics can still arise from a differential gain that varies over shorter periods. Differential gain systematics lead to a monopole T to P leakage that corresponds to γ_1 and γ_2. In Figure 17(c), we show the spectra for γ_1, γ_2, EE, and BB. Compared to the detector angle rotation and gain variation simulations (Figures 17(a) and (b)), where the instrumental effects are constant in time but vary over detector pairs, time-varying gain mismatches generate distortion power that is distributed over a larger range of multipoles.

For the instrumental systematics caused by the beam mismatch between orthogonal pairs of detectors, we make use of the T to P leakage template from the beam map simulations described in BK–III and BK-XI. With the high signal-to-noise ratio far-field beam map measurements, the expected T to P leakage signal from the measured beam mismatch is simulated for both 95 and 150 GHz. Since the beam map simulations are constant in time, the standard differential pointing deprojection completely removes the dipole leakage in the template, and no signal is detected with d_1 and d_2. As a sanity check and to demonstrate the power of the quadratic estimators, in Figure 17(d), we show the d_1, d_2, q, BB, and EE spectra generated by the dipole component of the leakage signal without deploying the differential pointing deprojection filter. Without deprojection, d_1 and d_2 spectra can detect the leakage signal at the lowest multipole with a much higher signal-to-noise ratio compared to the EE and BB spectra. In addition, q also strongly detects the dipole leakage signal because of its high correlation with the d_1 and d_2 field.

In Table 9, we quantify the impact on the BB power from the four systematic simulations with an estimator ρ that represents the equivalent tensor-to-scalar ratio r level of the contamination (Keck Array & BICEP2 Collaborations XI 2019). The estimator is constructed in a similar way to the estimator for
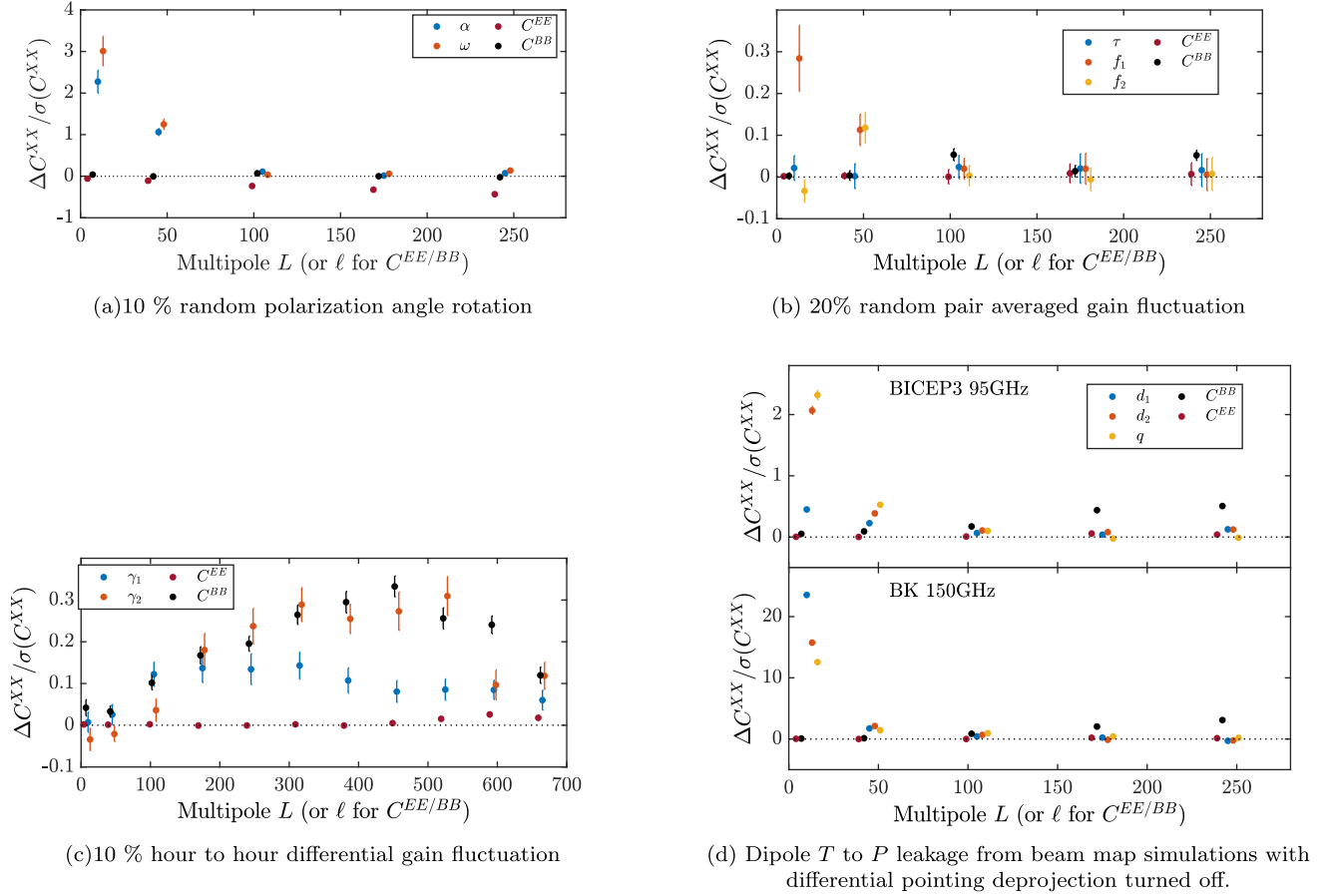
(a)10 % random polarization angle rotation

(b) 20% random pair averaged gain fluctuation

(c)10 % hour to hour differential gain fluctuation

(d) Dipole T to P leakage from beam map simulations with differential pointing deprojection turned off.

Figure 17. Relevant distortion field *EE* and *BB* difference spectra over the error bar $\Delta C^{XX}/\sigma(C^{XX})$ from the different systematics simulations. Panels (a) and (c) are identical to Figures 10 and 11 of Section 6.1.

Table 9
A Summary of the Four Systematics Simulations

Systematics	Sensitive Distortion Fields	Equivalent Level of r (ρ)	Sensitivity Ratio
B3 $10°$ random polarization angle rotation	α, ω	$<5.4 \times 10^{-4}$	20
B3 20% pair-averaged gain fluctuation	f_1, f_2	$<4.7 \times 10^{-4}$	3.9
B3 10% time-varying differential gain	γ_1, γ_2	$<1.2 \times 10^{-3}$	1.2
B3 95 GHz dipole T to P leakage (no deproj.)	d_1, d_2, q	6.4×10^{-3}	2.6
150 GHz dipole T to P leakage (no deproj.)	d_1, d_2, q	8.6×10^{-2}	4.2

Note. The level of *BB* power from the systematics simulations is characterized by ρ, the equivalent level of r contamination. The sensitivity ratio shows the detection significance of the distortion field quadratic estimators versus the *BB* spectrum at measuring the systematics. A ratio larger than 1 means that the quadratic estimators are more sensitive to the systematic effect. Note that the dipole T to P leakage shown here is the case without the differential pointing deprojection.

the lensing amplitude in Equation (37),

$$\rho = \frac{\sum_{bb'} \hat{C}_b \mathrm{Cov}_{bb'}^{-1} C_{b'}^{r=1}}{\sum_{bb'} C_b^{r=1} \mathrm{Cov}_{bb'}^{-1} C_{b'}^{r=1}}, \quad (B1)$$

where $\hat{C}_b$ are the *BB* bandpowers from the systematics simulations, $C_b^{r=1}$ is the mean *BB* bandpower for an $r=1$ signal, and $\mathrm{Cov}_{bb'}$ is the *BB* bandpower covariance matrix of the lensed-ΛCDM+dust+noise simulations. Even with the conservatively high levels of systematics in our simulations, the ρ estimates are relatively low at $\lesssim 1 \times 10^{-3}$. Note that the large ρ value for T to P dipole leakage is for the case without differential pointing deprojection shown just for demonstration.

In the main line analysis with deprojection enabled, the dipole T to P leakage will be entirely filtered out.

From the distortion and *BB* bandpowers in Figure 17, it is evident that the relevant distortion spectra are able to detect the systematics with higher significance compared to the *BB* spectrum. Applying the same formalism described by Equation (58) and using the mean systematics bandpowers as the fiducial C_b^f, we again evaluate the sensitivity ratio to compare the performance of quadratic estimators versus *BB* spectra. When the sensitivity ratio is greater than 1, the quadratic estimator is more sensitive than the *BB* power spectra in detecting the systematics. In Table 9, we show the sensitivity ratio of the combined sensitivity of all relevant distortion

spectra versus *BB* spectra. The sensitivity ratios for the four systematics considered here are all larger than 1, which means that the quadratic estimators for distortion fields are more sensitive than *BB* at detecting the spurious *B*-modes from these systematics. The ratio for random polarization angle rotation is particularly striking at 20 due to the fact that the random polarization rotation alters the *B*-mode while keeping the overall *BB* power roughly unchanged.

Appendix C
PTE Values for Alternate Choices of Analysis

In this appendix, we present the details and PTE values for the consistency checks listed in Section 5.4.1. The two frequency maps are examined independently for the consistency checks. For $\kappa(\hat{n})$, we derive an amplitude of the lensing potential for every analysis scenario. For all three fields $\tau(\hat{n})/\alpha(\hat{n})/\kappa(\hat{n})$, we evaluate the χ^2 PTEs of whether the different choices of analysis lead to the same conclusion as the baseline result, i.e., consistent with the lensed-ΛCDM+dust +noise simulations, and also whether the different choices of analysis are consistent with the baseline.

The χ^2 PTE for comparing with lensed-ΛCDM simulations is exactly the same as Equations (47) and (48); therefore, the

PTE values for the baseline case are the same as the numbers in Table 6. All of the PTEs in the "versus lensed-ΛCDM" columns in Table 10 are reasonable, which means that the main science result, i.e., that $C_L^{\alpha\alpha}$, $C_L^{\tau\tau}$, and $C_L^{\kappa\kappa}$ are consistent with lensed-ΛCDM, is not sensitive to the different choices of analyses. For the consistency checks of alternate analysis choices versus baseline, we evaluate the difference of the bandpowers $\hat{C}_b^{dd}$ from the two analyses,

$$\Delta\hat{C}_b^{dd} = \hat{C}_b^{dd,\text{alt}} - \hat{C}_b^{dd,\text{baseline}}, \quad (C1)$$

where $\hat{C}_b^{dd,\text{alt}}$ are the reconstructed bandpowers from the alternate analysis, and $\hat{C}_b^{dd,\text{baseline}}$ are the bandpowers from the baseline analysis. The χ^2 statistics is constructed as

$$\chi^2_{\text{alt}} = \sum_{bb'}(\Delta\hat{C}_b - \langle\Delta C_b\rangle)\text{Cov}_{bb'}^{-1}(\Delta\hat{C}_{b'} - \langle\Delta C_{b'}\rangle), \quad (C2)$$

where $\text{Cov}_{bb'}$ is the bandpower covariance matrix from the difference bandpowers from simulations, and $\langle\Delta C_b\rangle$ is the mean difference bandpowers of simulations. The PTE values are then calculated by comparing the χ^2_{alt} of the data versus simulations.

Table 10
The Results for Alternate Analysis Choices for $\alpha(\hat{n})$, $\tau(\hat{n})$, and $\kappa(\hat{n})$

	95 GHz			150 GHz		
	$A_L^{\phi\phi}$	versus Lensed-ΛCDM ($\alpha/\tau/\kappa$)	versus Baseline ($\alpha/\tau/\kappa$)	$A_L^{\phi\phi}$	versus Lensed-ΛCDM ($\alpha/\tau/\kappa$)	versus Baseline ($\alpha/\tau/\kappa$)
Baseline	0.88 ± 0.23	0.66/0.96/0.71	N/A	1.10 ± 0.33	0.35/0.83/1.00	N/A
$\ell_{\min} = 200$	0.88 ± 0.26	0.86/0.58/0.58	0.64/0.39/0.36	0.78 ± 0.36	0.57/0.45/0.80	0.73/0.31/0.26
$\ell_{\max}^B = 350$	0.89 ± 0.29	0.57/0.99/0.98	0.55/0.99/0.88	1.24 ± 0.42	0.38/0.95/1.00	0.44/0.99/0.93
$\ell_{\max} = 400$	0.65 ± 0.36	0.41/0.95/0.94	0.44/0.83/0.93	1.68 ± 0.48	0.15/0.25/0.20	0.49/0.12/0.08
No diff. ellipticity	0.88 ± 0.23	0.64/0.94/0.73	N/A	1.07 ± 0.33	0.42/0.88/1.00	N/A

Note. Here $A_L^{\phi\phi}$ is the measured amplitude of the lensing potential, "versus lensed-ΛCDM" shows the χ^2 PTE values of the observed bandpowers compared to the bandpowers from lensed-ΛCDM+dust+noise simulations, and "versus baseline" shows the χ^2 PTE values when comparing the bandpowers of the alternate analysis with the baseline analysis.

Appendix D
Exploration of Alternate Foreground Models

In Section 4.2, we set a lower bound on the B-mode multipole input with $\ell_{\min}^B = 100, 150$ for 95 and 150 GHz, respectively, to avoid B-modes that have significant contribution from the galactic foreground. Here we extend the analysis to simulations using some alternate foreground models to explore the effects of different models of galactic foreground on distortion field reconstructions. The models considered are described in Appendix E.4 of BK–XIII and BK–X.

Our basic set of simulations includes Gaussian realizations of dust. One model extends the Gaussian foreground to contain frequency decorrelation (labeled G. Decorr.), which should have no effect in this assessment, since we study one frequency at a time. We also extend the Gaussian foreground to have amplitude modulation, where the Gaussian full-sky realizations are multiplied by the square root of maps of degree-scale BB power measured from small patches of the Planck 353 GHz map (labeled G. amp. mod.).

A suite of third-party foreground models with only one realization available is also considered: the PySM models 1, 2, and 3 (Thorne et al. 2017); the MHD model (Kritsuk et al. 2017, 2018); the MKD model (Martínez-Solaeche et al. 2018); and the Vansyngel model (Vansyngel et al. 2017). We find that many of the alternate foreground models would cause significant bias on the reconstructed spectra without the realization-dependent method. However, with the realization-dependent method, the reconstructed spectra to first order are not sensitive to a change in the EE and BB power, and the shifts become negligible. This suggests that the dust models considered here do not have a significant impact on the reconstructed distortion fields but mainly affect the distortion field analysis through altering the overall level of EE and BB power. In Figure 18, we summarize the mean bandpower shift in the reconstructed distortion spectra over bins for each distortion field, $\langle \Delta C_b^{DD}/\sigma(C_b^{DD})\rangle_b$. Note that the PySM models predict considerably higher dust power in the BK field than is actually observed. The mean shift in bandpowers for distortion fields for which we expect and measure a cosmological signal is negligible.
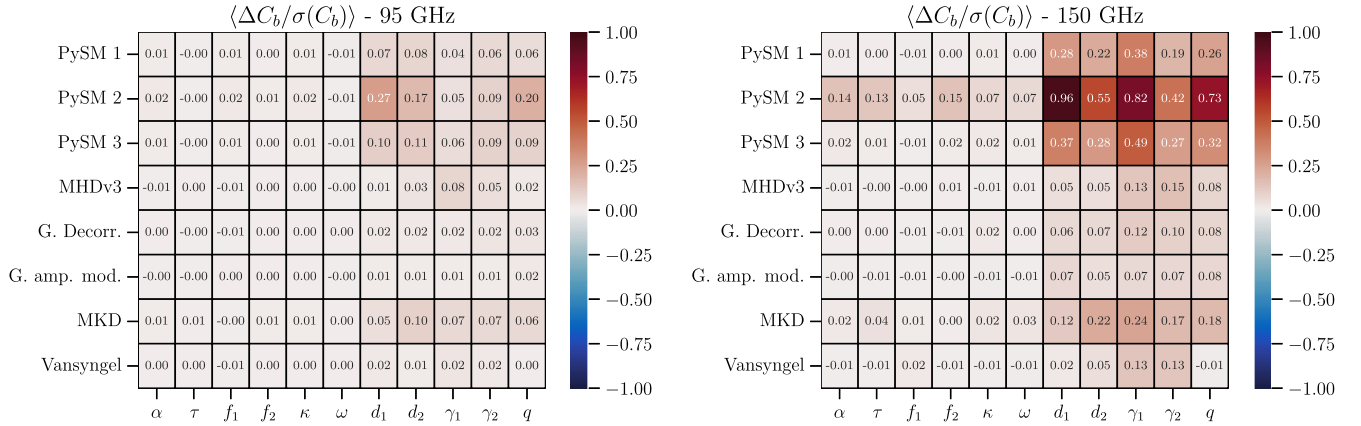

Figure 18. Mean bandpower deviation $\langle \Delta C_b/\sigma(C_b)\rangle$ averaged over all bins for each of the 11 distortion fields. The choice of bins is the same as in Figures 14 and 16.

Appendix E
Detection of Polarized Point Sources

In this appendix, we provide an explanation of why the *TB* distortion spectra are sensitive to polarized point sources. We further derive *EB*/*BB*/*TB* point-source estimators (labeled as $\langle EBEB \rangle/\langle BBBB \rangle/\langle TBTB \rangle$ later in this appendix) of the same quadratic form as Equation (19) that are designed specifically to detect point sources. Compared to detecting point sources with excess *B*-mode power, the point-source quadratic estimators are more sensitive when the flux from a few individual sources dominates. Additionally, the *TB* point-source estimator is more sensitive than the polarization-only estimators when the polarization fraction is low. Since most of the polarized point-source flux comes from the few brightest sources with a low polarization fraction ($\approx$2%–3%; Tucci & Toffolatti 2012), we expect the *TB* estimators to be most sensitive at detecting polarized point sources in the BK data.

There has not been much discussion in the literature about the detection of point sources from temperature and polarization correlations. The main reason is that the random polarization angles of point sources imply that the two-point functions C_ℓ^{TQ} and C_ℓ^{TU} from point sources are zero, on average (Tucci & Toffolatti 2012). However, if we go beyond the two-point functions, the four-point functions such as $C_L^{\gamma_1 \gamma_1}$ and $C_L^{\gamma_2 \gamma_2}$ that are constructed from $\langle TBTB \rangle$ correlations do not cancel out when averaged over random point-source polarization angle orientations, and they are evidently sensitive at detecting polarized point sources, as shown in Table 5.

A single linearly polarized point source generates $\langle T(\hat{n})Q(\hat{n}) \rangle$ or $\langle T(\hat{n})U(\hat{n}) \rangle$ correlations at the location of the source. On the other hand, it produces no $\langle T(\hat{n})B(\hat{n}) \rangle$ correlations if we assume a radially symmetric and thus even-parity profile. However, with the filter functions in Table 2 applied, the contribution from a polarized point source to γ_1 and γ_2 will be nonzero. The power spectra of the quadratic *TB* estimators for γ_1 and γ_2 are effectively measuring the four-point $\langle TQTQ \rangle$ and $\langle TUTU \rangle$ correlations only using the *B*-mode and not the *E*-mode component of the CMB polarization signal. Compared to a direct correlation of the full $\langle TQTQ \rangle$ and $\langle TUTU \rangle$, the $\gamma_{1/2}$ *TB* estimators will be more sensitive to the point sources because the sample variance is much lower without the contributions from the bright ΛCDM *E*-modes.

The *TB* quadratic estimators with filter functions in Table 2 are designed to measure the distortion fields and not point sources. It is possible to design better estimators of the same quadratic form as Equation (19) that specifically target point sources. The point-source estimators from the CMB temperature signal are described in Osborne et al. (2014), and Namikawa & Takahashi (2014b) extended the formalism to include polarization-only point-source estimators. Here we extend the point-source estimators described in Section 3.1.2 of Namikawa & Takahashi (2014b) to include temperature and polarization correlation. We will only consider the "1 source terms" (source terms containing only a single source, see Section III of Osborne et al. 2014), ignoring any contribution from clustering of the sources.

Let us consider a point-source model with sky signal $[T^p(\hat{n}), U^p(\hat{n}), Q^p(\hat{n})]$ that is uncorrelated between pixels. Assuming the point sources are partially polarized with random

orientations, we have

$$Q^p(\hat{n}) = g_1(\hat{n})T^p(\hat{n}), \tag{E1}$$

$$U^p(\hat{n}) = g_2(\hat{n})T^p(\hat{n}), \tag{E2}$$

where

$$\langle g_1(\hat{n})g_2(\hat{n}') \rangle_{\mathrm{src}} = 0, \tag{E3}$$

$$\langle g_1(\hat{n})T^p(\hat{n}') \rangle_{\mathrm{src}} = 0. \tag{E4}$$

With $S(\hat{n}) = T^p(\hat{n})^2$, $\sigma_1(\hat{n}) = g_1(\hat{n})^2$, and $\sigma_2(\hat{n}) = g_1(\hat{n})^2$,

$$\langle T^p(\hat{n})T^p(\hat{n}') \rangle_{\mathrm{src}} = \langle S(\hat{n}) \rangle_{\mathrm{src}} \delta(\hat{n} - \hat{n}'), \tag{E5}$$

$$\langle g_1(\hat{n})g_1(\hat{n}') \rangle_{\mathrm{src}} = \langle \sigma_1(\hat{n}) \rangle_{\mathrm{src}} \delta(\hat{n} - \hat{n}'), \tag{E6}$$

$$\langle g_2(\hat{n})g_2(\hat{n}') \rangle_{\mathrm{src}} = \langle \sigma_2(\hat{n}) \rangle_{\mathrm{src}} \delta(\hat{n} - \hat{n}'), \tag{E7}$$

where the brackets stand for the mean over the point-source realizations given our point-source model, and $\langle \sigma_1(\hat{n}) \rangle_{\mathrm{src}} = \langle \sigma_2 \hat{n} \rangle_{\mathrm{src}}$.

Recall that a correlation of Equation (A9) would lead to a minimum variance quadratic estimator of Equation (19). Therefore, we evaluate $\langle X_{l_1} X'_{l_2} \rangle_{\mathrm{CMB}}$ with $XX' = EE, EB, BB, TB$. Note that we are taking the ensemble average over the CMB realizations here. With $[E_l^p \pm iB_l^p] = \int d^2\hat{n} e^{-i\hat{n}\cdot l}[Q^p \pm iU^p](\hat{n})e^{\mp 2i\phi_l}$, we have

$$\langle T_{l_1}T_{l_2} \rangle_{\mathrm{CMB}} = S_L, \tag{E8}$$

$$\langle E_{l_1}E_{l_2} \rangle_{\mathrm{CMB}} = [S\sigma_1]_L \cos(2\phi_{l_1})\cos(2\phi_{l_2}) + [S\sigma_2]_L \sin(2\phi_{l_1})\sin(2\phi_{l_2}), \tag{E9}$$

$$\langle B_{l_1}B_{l_2} \rangle_{\mathrm{CMB}} = [S\sigma_1]_L \cos(2\phi_{l_1})\cos(2\phi_{l_2}) + [S\sigma_2]_L \sin(2\phi_{l_1})\sin(2\phi_{l_2}), \tag{E10}$$

$$\langle E_{l_1}B_{l_2} \rangle_{\mathrm{CMB}} = -[S\sigma_1]_L \cos(2\phi_{l_1})\sin(2\phi_{l_2}) + [S\sigma_2]_L \sin(2\phi_{l_1})\cos(2\phi_{l_2}), \tag{E11}$$

$$\langle T_{l_1}B_{l_2} \rangle_{\mathrm{CMB}} = [Sg_2]_L \cos(2\phi_{l_2}) - [Sg_1]_L \sin(2\phi_{l_2}), \tag{E12}$$

where $[S\sigma_i]_L = \int d^2\hat{n} e^{-i\hat{n}\cdot L}S(\hat{n})\sigma_i(\hat{n})$ and similarly for $[Sg_i]_L$. If we consider only the common modes of $S\sigma_1$ and $S\sigma_2$, the filter functions of the *EE*, *EB*, and *BB* point-source estimators are $f_{l_1,l_2}^{EE} = f_{l_1,l_2}^{BB} = \cos(2\phi_{l_1} - 2\phi_{l_2})$ and $f_{l_1,l_2}^{EB} = \sin(2\phi_{l_1} - 2\phi_{l_2})$. For the *TB* estimator, we have $f_{l_1,l_2}^{TB,1} = -\sin(2\phi_{l_2})$ and $f_{l_1,l_2}^{TB,2} = \cos(2\phi_{l_2})$, which probe $\langle TQTQ \rangle$ and $\langle TUTU \rangle$, respectively. It is also possible to compute the cross-spectrum of the two *TB* estimators to probe $\langle TQTU \rangle$. Note that the two *TB* point-source estimators for Sg_1 and Sg_2 have the same geometric terms ($\sin(2\phi_{l_2})$ and $\cos(2\phi_{l_2})$) as the distortion field estimators for $\gamma_1(\hat{n})$ and $\gamma_2(\hat{n})$. The only difference is that there is no longer a C_ℓ^{TT} factor in the filter function *f*. This change in the weights result in a factor of $\sim$2 sensitivity improvement at detecting point sources in the BICEP3 95 GHz maps.

The polarized point sources also produce excess C_ℓ^{BB} power, especially at higher ℓ. With the same method as Section 6.2, we compare the signal-to-noise ratio of detecting the polarized point sources with the four-point point-source estimators versus the two-point C_ℓ^{BB} by running simulations. The parameter spaces explored are the polarized point-source flux for individual sources (from 2 to 16 mJy) and the fraction of polarization (from 0.5% to 8%). For each set of parameters, we
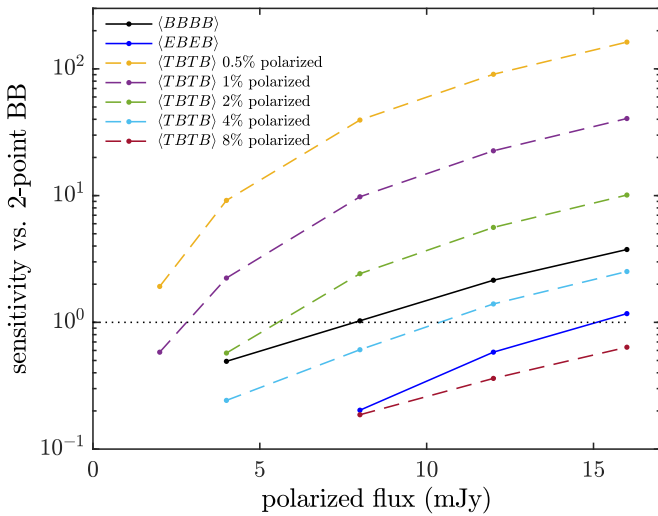
Figure 19. Signal-to-noise ratio for detecting the point sources of the different four-point estimators compared to two-point C_ℓ^{BB} power in the BK18 95 GHz simulations. A sensitivity ratio larger than 1 on the *y*-axis means that the four-point estimator is more sensitive than the *BB* power spectrum at detecting that population (polarized flux and fraction) of point sources. Here $\langle EEEE \rangle$ has too low a sensitivity to be probed by our simulations and is therefore not shown.

generated 99 realizations of 40 point sources with the same flux at random locations in the map and random polarization orientations. In Figure 19, we find that all of the point-source estimators (four-point functions) have a sensitivity that scales as flux^2 relative to the two-point function C_ℓ^{BB}, since the signal in a four-point function is $\propto$ flux^4, while the signal in a two-point function is $\propto$ flux^2. The $\langle BBBB \rangle$ estimator is much more sensitive than the $\langle EBEB \rangle$ and $\langle EEEE \rangle$ estimators, since $\langle BBBB \rangle$ does not have the large sample variance contribution from ΛCDM *E*-modes. Additionally, the $\langle TBTB \rangle$ estimator is more sensitive than the polarization-only point-source estimators when the polarization fraction is small. When the point sources are less than $\approx$3% polarized, the $\langle TBTB \rangle$ estimator is more sensitive compared to the $\langle BBBB \rangle$ estimator.

ORCID iDs

R. Basu Thakur ⓘ https://orcid.org/0000-0002-3351-3078
C. A. Bischoff ⓘ https://orcid.org/0000-0001-9185-6514
V. Buza ⓘ https://orcid.org/0000-0002-1345-4322
J. R. Cheshire IV ⓘ https://orcid.org/0000-0002-1630-7854
A. Cukierman ⓘ https://orcid.org/0000-0002-7471-719X
M. Dierickx ⓘ https://orcid.org/0000-0002-3519-8593
J. P. Filippini ⓘ https://orcid.org/0000-0001-8217-6832
D. C. Goldfinger ⓘ https://orcid.org/0000-0001-5268-8423
P. Grimes ⓘ https://orcid.org/0000-0001-9292-6297
G. Halal ⓘ https://orcid.org/0000-0003-2221-3018
M. Halpern ⓘ https://orcid.org/0000-0002-1760-0868
H. Hui ⓘ https://orcid.org/0000-0001-5812-1903
K. D. Irwin ⓘ https://orcid.org/0000-0002-2998-9743
J. Kang ⓘ https://orcid.org/0000-0002-3470-2954
K. S. Karkare ⓘ https://orcid.org/0000-0002-5215-6993
K. Lau ⓘ https://orcid.org/0000-0002-6445-2407
L. Moncelsi ⓘ https://orcid.org/0000-0002-4242-3015
T. Namikawa ⓘ https://orcid.org/0000-0003-3070-9240
M. Petroff ⓘ https://orcid.org/0000-0002-4436-4215
C. Pryke ⓘ https://orcid.org/0000-0003-3983-6668
B. Racine ⓘ https://orcid.org/0000-0001-8861-3052
C. Vergès ⓘ https://orcid.org/0000-0002-3942-1609
J. Willmert ⓘ https://orcid.org/0000-0002-6452-4693
L. Zeng ⓘ https://orcid.org/0000-0001-6924-9072

References

Ade, P. A. R., Arnold, K., Atlas, M., et al. 2015, PhRvD, 92, 123509
BICEP2 Collaboration I 2014, PhRvL, 112, 241101
BICEP2 Collaboration II 2014, ApJ, 792, 62
BICEP2 Collaboration III 2015, ApJ, 814, 110
BICEP2/Keck & Planck Collaborations 2015, PhRvL, 114, 101301
Battye, R. A., Browne, I. W. A., Peel, M. W., Jackson, N. J., & Dickinson, C. 2011, MNRAS, 413, 132
Beck, D., Errard, J., & Stompor, R. 2020, JCAP, 2020, 030
Beck, D., Fabbian, G., & Errard, J. 2018, PhRvD, 98, 043512
Bianchini, F., Wu, W. L. K., Ade, P. A. R., et al. 2020, PhRvD, 102, 083504
BICEP/Keck Collaboration XIII 2021, PhRvL, 127, 151301
Böhm, V., Sherwin, B. D., Liu, J., et al. 2018, PhRvD, 98, 123510
Bortolami, M., Billi, M., Gruppuso, A., Natoli, P., & Pagano, L. 2022, JCAP, 2022, 075
Caldwell, R. R., Gluscevic, V., & Kamionkowski, M. 2011, PhRvD, 84, 043504
Carroll, S. M., Field, G. B., & Jackiw, R. 1990, PhRvD, 41, 1231
Carron, J., Mirmelstein, M., & Lewis, A. 2022, JCAP, 2022, 039
Contreras, D., Boubel, P., & Scott, D. 2017, JCAP, 2017, 046
Cooray, A., Kamionkowski, M., & Caldwell, R. R. 2005, PhRvD, 71, 123527
De, S., Pogosian, L., & Vachaspati, T. 2013, PhRvD, 88, 063527
Dodelson, S., Rozo, E., & Stebbins, A. 2003, PhRvL, 91, 021301
Dvorkin, C., Hu, W., & Smith, K. M. 2009, PhRvD, 79, 107302
Fabbian, G., Calabrese, M., & Carbone, C. 2018, JCAP, 2018, 050
Faúndez, M. A., Arnold, K., Baccigalupi, C., et al. 2020, ApJ, 893, 85
Gluscevic, V., Hanson, D., Kamionkowski, M., & Hirata, C. M. 2012, PhRvD, 86, 103529
Gluscevic, V., Kamionkowski, M., & Hanson, D. 2013, PhRvD, 87, 047303
Gorce, A., Douspis, M., & Salvati, L. 2022, A&A, 662, A122
Gruppuso, A., Molinari, D., Natoli, P., & Pagano, L. 2020, JCAP, 2020, 066
Hamimeche, S., & Lewis, A. 2008, PhRvD, 77, 103013
Hanson, D., Challinor, A., Efstathiou, G., & Bielewicz, P. 2011, PhRvD, 83, 043005
Hirata, C. M., & Seljak, U. 2003, PhRvD, 68, 083002
Hu, W. 2000, ApJ, 529, 12
Hu, W., Hedman, M. M., & Zaldarriaga, M. 2003, PhRvD, 67, 043004
Hu, W., & Okamoto, T. 2002, ApJ, 574, 566
Keck Array & BICEP2 Collaborations IX. 2017, PhRvD, 96, 102003
Keck Array & BICEP2 Collaborations VI 2016, PhRvL, 116, 031302
Keck Array & BICEP2 Collaborations VII 2016, ApJ, 825, 66
Keck Array & BICEP2 Collaborations VIII 2016, ApJ, 833, 228
Keck Array & BICEP2 Collaborations X 2018, PhRvL, 121, 221301
Keck Array & BICEP2 Collaborations XI 2019, ApJ, 884, 114
Kesden, M., Cooray, A., & Kamionkowski, M. 2003, PhRvD, 67, 123507
Kritsuk, A. G., Flauger, R., & Ustyugov, S. D. 2018, PhRvL, 121, 021104
Kritsuk, A. G., Ustyugov, S. D., & Norman, M. L. 2017, NJPh, 19, 065003
Lembo, M., Fabbian, G., Carron, J., & Lewis, A. 2022, PhRvD, 106, 023525
Marsh, D. J. E. 2016, PhR, 643, 1
Martínez-Solaeche, G., Karakci, A., & Delabrouille, J. 2018, MNRAS, 476, 1310
Mirmelstein, M., Fabbian, G., Lewis, A., & Peloton, J. 2021, PhRvD, 103, 123540
Monsalve, R. A., Rogers, A. E. E., Bowman, J. D., & Mozdzen, T. J. 2017, ApJ, 847, 64
Namikawa, T. 2018, PhRvD, 97, 063505
Namikawa, T., Guan, Y., Darwish, O., et al. 2020, PhRvD, 101, 083527
Namikawa, T., Hanson, D., & Takahashi, R. 2013, MNRAS, 431, 609
Namikawa, T., & Takahashi, R. 2014a, MNRAS, 438, 1507
Namikawa, T., & Takahashi, R. 2014b, MNRAS, 438, 1507
Namikawa, T., Yamauchi, D., & Taruya, A. 2012, JCAP, 2012, 007
Osborne, S. J., Hanson, D., & Doré, O. 2014, JCAP, 2014, 024
Planck Collaboration, Ade, P. A. R., Aghanim, N., et al. 2016a, A&A, 594, A15
Planck Collaboration, Adam, R., Aghanim, N., et al. 2016b, A&A, 596, A108
Planck Collaboration, Ade, P. A. R., Aghanim, N., et al. 2014, A&A, 571, A16
Planck Collaboration, Aghanim, N., Akrami, Y., et al. 2020a, A&A, 641, A8
Planck Collaboration, Aghanim, N., Akrami, Y., et al. 2020b, A&A, 641, A6
Planck Collaboration, Aghanim, N., Akrami, Y., et al. 2021, A&A, 652, C4

Paoletti, D., Chluba, J., Finelli, F., & Rubiño-Martin, J. A. 2022, MNRAS, 517, 3916

Pratten, G., & Lewis, A. 2016, JCAP, 2016, 047

Reichardt, C. L., Patil, S., Ade, P. A. R., et al. 2021, ApJ, 908, 199

Sherwin, B. D., van Engelen, A., Sehgal, N., et al. 2017, PhRvD, 95, 123529

Story, K. T., Hanson, D., Ade, P. A. R., et al. 2015, ApJ, 810, 50

Sunyaev, R. A., & Zeldovich, I. B. 1980, ARA&A, 18, 537

Sunyaev, R. A., & Zeldovich, Y. B. 1970, Ap&SS, 7, 3

Thorne, B., Dunkley, J., Alonso, D., & Næss, S. 2017, MNRAS, 469, 2821

Tucci, M., & Toffolatti, L. 2012, AdAst, 2012, 624987

Vansyngel, F., Boulanger, F., Ghosh, T., et al. 2017, A&A, 603, A62

Williams, J., McCallum, N., Rotti, A., et al. 2021, JCAP, 2021, 016

Wu, W. L. K., Mocanu, L. M., Ade, P. A. R., et al. 2019, ApJ, 884, 70

Yadav, A., Pogosian, L., & Vachaspati, T. 2012, PhRvD, 86, 123009

Yadav, A. P. S., Su, M., & Zaldarriaga, M. 2010, PhRvD, 81, 063512

Yamauchi, D., Takahashi, K., Sendouda, Y., & Yoo, C.-M. 2012, PhRvD, 85, 103515

Zaldarriaga, M., & Seljak, U. 1998, PhRvD, 58, 023003

Zucca, A., Li, Y., & Pogosian, L. 2017, PhRvD, 95, 063506